

A mechanically consistent model for fluid-structure interactions with contact including seepage

Erik Burman, Miguel A. Fernández, Stefan Frei and Fannie M. Gerosa

March 23, 2021

Abstract

We present a new approach for the mechanically consistent modelling and simulation of fluid-structure interactions with contact. The fundamental idea consists of combining a relaxed contact formulation with the modelling of seepage through a porous layer of co-dimension 1 during contact. For the latter, a Darcy model is considered in a thin porous layer attached to a solid boundary in the limit of infinitesimal thickness. In combination with a relaxation of the contact conditions the computational model is both mechanically consistent and simple to implement. We analyse the approach in detailed numerical studies with both thick- and thin-walled solids, within a fully Eulerian and an immersed approach for the fluid-structure interaction and using fitted and unfitted finite element discretisations.

1 Introduction

The design and analysis of computational methods for systems where several solids are immersed in a fluid and that can come into contact is an outstanding problem. Already fluid-structure interaction (FSI) without contact is challenging due to the moving geometries and the stiff coupling between the solid and the fluid systems. If contact between solids is to be modelled as well, the complexity increases drastically. Indeed, the addition of contact introduces several important aspects, such as:

- Topological changes in the fluid domain;
- Non-linearly changing interface conditions: The interface condition changes from a fluid-solid interaction to a solid-solid contact problem which is described by variational inequalities;
- Important differences in the characteristic scales of the different physical phenomena: The contact represents a singular phenomenon in time. In three space dimensions, the contact zone is a two dimensional subset of the solid-solid interface and there is also a one dimensional subset of the contact zone forming the solid-solid-fluid line.

Ideally, a computational method should be consistent with the physics, be amenable to mathematical analysis and convenient to implement in a computational software.

In the case of fluid-structure interaction with contact, an additional complication is that it is unclear what mathematical modelling will produce the best results. Indeed, it is known that a naive imposition of no-slip conditions on one of the boundaries of a solid will prevent contact of smooth bodies in the solution of the PDE system [Hesla, 2004, Hillaire, 2007, Gerard-Varet et al., 2015], contrary to what is observed in experiments [Hagemeier et al., 2020].

Therefore, the design of computational methods for FSI-contact problems can not be completely dissociated from the problem of modelling, but it is important to keep a certain flexibility concerning the contact modelling to be able to include a wide range of physics, depending on the characteristics of the considered system. In this work, we will build on previous work for FSI with contact [Burman et al., 2020a]. There, recent techniques merging the ideas of weak imposition of fluid-structure interface conditions [Hansbo et al., 2004, Burman and Fernández, 2014] with a multiplier free formulation for contact [Chouly and Hild, 2013] were developed, leading to an automatic handling of both fluid-solid and solid-solid coupling conditions. The main idea was to merge different versions of Nitsche's method using an augmented Lagrangian formulation for variational inequalities dating back to Rockafellar [Rockafellar, 1973]. The resulting method is consistent and shown in numerical examples to be both accurate and robust. It can also easily be combined with tools developed to facilitate the handling of the moving

interfaces such as cutFEM [Burman et al., 2015, Burman and Fernández, 2014], XFEM [Moës et al., 1999], GFEM [Babuška et al., 2004] or fitted finite element approaches [Frei and Richter, 2014].

Already in [Burman et al., 2020a] some modelling aspects were developed. In order to avoid the singularity of vanishing pressure in the contact zone the fluid was extended into the solid in a porous medium model. Alternatively, the distance between the contacting bodies can be lower bounded by some small value (proportional to the mesh size) representing the idea that a fluid layer always remain between the contacting bodies. A similar approach was taken in [Ager et al., 2019], but here the physical modelling went further, introducing porous layers on the solids and modelling the full 3D poro-elastic fluid-structure interaction with contact. In the computational model for contact, a Lagrange multiplier technique was applied in contrast to the Nitsche-approach in [Burman et al., 2020a]. In [Zonca et al., 2020] a polygonal DG discretisation is used within a penalty method in combination with a switch between Navier-slip to slip conditions to enable the transition to contact. The recent work [Ager et al., 2020] showcases the potential of combining the Nitsche FSI-contact conditions of [Burman et al., 2020a] with the FSI-cutFEM approach from [Burman and Fernández, 2014] using realistic physical models in some impressive computational examples.

In the present work, we wish to build on the ideas of [Burman et al., 2020a] by considering a model for contact with seepage due to microscopic roughness of the contacting bodies. Let $\Omega \subset \mathbb{R}^d$ for $d = 2, 3$ be the overall domain consisting of fluid and solid subdomains. The seepage is modelled by the introduction of a $d - 1$ -dimensional porous layer that adheres to a solid boundary, where contact might take place. This can be considered as a generalised boundary condition, or a bulk surface coupling in the spirit of [Elliott and Ranner, 2013]. In our case, however, the free-flow Navier-Stokes' system is coupled to a surface Darcy equation. This model goes back to [Martin et al., 2005] and is of interest in its own right, as discussed in the note [Burman et al., 2021]. By combining this porous layer approach for seepage with the contact approach of [Burman et al., 2020a], herein extended to the case of thin-walled solids, we obtain an approach that inherits the simplicity, accuracy and robustness of [Burman et al., 2020a], but provides a mechanically consistent model for fluid-structure interaction with contact.

We implement the approach using different coordinate systems, discretisations and solid models. Concerning coordinate systems, we consider both an Immersed approach going back to Peskin [Peskin, 1972] as well as a Fully Eulerian approach [Dunne, 2006, Cottet et al., 2008, Richter, 2013, Frei, 2016]. For discretisation, we use the unfitted finite element method of [Hansbo et al., 2004, Burman and Fernández, 2014, Alauzet et al., 2016] and the two-scale interface fitting approach of [Frei and Richter, 2014]. We illustrate the modelling capacity in a series of computational examples in two dimensions, including a beam solid model and a thick-walled solid model.

Indeed, depending on if no-slip conditions are imposed or if the porous medium approach proposed here is used the approximations will converge to different solutions for mesh size $h \rightarrow 0$. If we consider the case of a bouncing ball the use of no-slip conditions will lead to a sequence of solutions that converge to a ball that does not bounce, whereas the solutions obtained with the porous medium approach converge to a certain bouncing height that depends on the parameters of the Darcy model. Recent comparisons of computational methods with experimental studies ([Hagemeier et al., 2020], [von Wahl et al., 2020]) confirm that the second behavior is the physical one. Of course the parameters of the model need to be fixed through experimental studies, or otherwise.

An outline of the paper is as follows. In Section 2, we introduce the Navier-Stokes-Darcy coupling as well as the FSI-contact model. The variational formulation and the discretisation based on Nitsche's method is described in Section 3. In Section 4 we give detailed numerical studies both in the case of a beam model and a thick solid. We conclude in Section 5.

2 Equations

In this section, we derive the Navier-Stokes-Darcy coupling, and subsequently the equations for fluid-structure-porous-contact interaction. For simplicity, we will consider that contact takes place at a given fixed plane surface. This can be either an exterior rigid wall or a symmetry boundary within the fluid domain, which is relevant for example in the case of contact between two symmetric valves. The case of to two-body contact is not considered here.

The fluid equations in $\Omega^f(t) \subset \mathbb{R}^d$ will be coupled to a fixed $(d - 1)$ -dimensional porous layer Σ_p on the exterior boundary, where contact might take place. The fluid is described by the Navier-Stokes equations in Eulerian formalism and the structure by a possibly non-linear solid model. We consider both $(d - 1)$ -dimensional thin-walled solids and d -dimensional thick-walled solids.

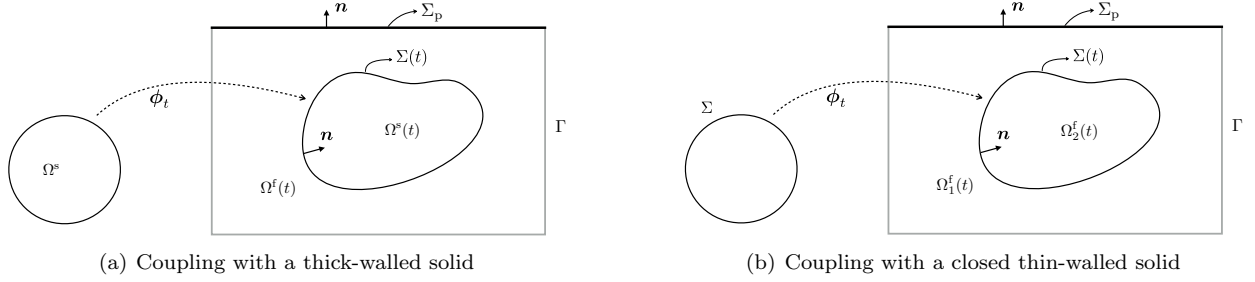


Figure 1: Geometric configurations of the fluid and solid domains.

2.1 Problem setting

Let $\Omega = \overline{\Omega^s(t)} \cup \Omega^f(t) \subset \mathbb{R}^d$ be a current configuration of the complete domain of interest, with boundary $\partial\Omega := \Gamma \cup \Sigma_p$, where Σ_p denotes the part of the boundary where contact might take place (see Figure 1). There, a thin porous fluid layer is considered. The solid domain $\Omega^s(t)$ can be either a surface (actually the solid mid-surface) or a domain with positive volume in \mathbb{R}^d in the case of the coupling with a thick-walled solid. The current fluid-structure interface is denoted by $\Sigma(t)$ and coincides with $\Omega^s(t)$ in the case of a thin-walled solid. The corresponding reference configurations are denoted by Σ and Ω^s .

The structure is allowed to move freely within the domain Ω . The current position of the interface $\Sigma(t)$ and the solid domain $\Omega^s(t)$ are described in terms of a deformation map $\phi : \Omega^s \times \mathbb{R}^+ \rightarrow \mathbb{R}^d$ such that $\Omega^s(t) = \phi(\Omega^s, t)$ and $\Sigma(t) = \phi(\Sigma, t)$, with $\phi := \mathbf{I}_{\Omega^s} + \mathbf{d}$ and where \mathbf{d} denotes the solid displacement. To simplify the notation we will refer to $\phi_t := \phi(\cdot, t)$, so that we can also write $\Omega^s(t) = \phi_t(\Omega^s)$, $\Sigma(t) = \phi_t(\Sigma)$. The fluid domain is time-dependent, namely $\Omega^f(t) := \Omega \setminus (\Omega^s(t) \cup \Sigma(t)) \subset \mathbb{R}^d$ with boundary $\partial\Omega^f(t) = \Sigma(t) \cup \Gamma \cup \Sigma_p$. In the case of a closed thin-walled structure, the solid domain $\Omega^s(t)$ divides $\Omega^f(t)$ into two subdomains $\Omega^f(t) = \Omega_1^f(t) \cup \Omega_2^f(t)$, with respective unit normals $\mathbf{n}_1 := \mathbf{n}$ and $\mathbf{n}_2 := -\mathbf{n}$, as shown in Figure 1(b). Similarly, in the case of a thick-walled solid, the interface $\Sigma(t)$ divides Ω into a solid part $\Omega^s(t)$ and a fluid part $\Omega^f(t)$. We write $H_\Gamma^1(\Omega)$ for the first-order Sobolev space with vanishing trace on $\Gamma \subset \partial\Omega$.

For a given field f defined in Ω (possibly discontinuous across the interface), we can define its one-sided restrictions, denoted by f_1 and f_2 , as

$$f_1(\mathbf{x}) := \lim_{\xi \rightarrow 0^-} f(\mathbf{x} + \xi \mathbf{n}_1), \quad f_2(\mathbf{x}) := \lim_{\xi \rightarrow 0^-} f(\mathbf{x} + \xi \mathbf{n}_2),$$

for all $\mathbf{x} \in \Sigma(t)$, and the following jump and average operators across $\Sigma(t)$:

$$[[f]] := f_1 - f_2 \quad [[f\mathbf{n}]] := f_1\mathbf{n}_1 + f_2\mathbf{n}_2, \quad \{f\} := \frac{1}{2}(f_1 + f_2). \quad (1)$$

In the case of a thin structure that has a boundary inside the fluid domain (for example with a tip), these quantities can be defined similarly. For the details, we refer to [Alauzet et al., 2016] and Remark 3.1 below.

While the fluid and solid equations are standard and will be introduced in Section 2.3, we give some details on the porous medium model in the following section.

2.2 Porous medium model and Navier-Stokes-Darcy coupling

We consider the configuration sketched in Figure 2, where a thin porous layer $\Omega_p = \Sigma_p \times (-\frac{\epsilon_p}{2}, \frac{\epsilon_p}{2}) \in \mathbb{R}^d$ ($d = 2, 3$) with midsurface Σ_p is coupled to a surrounding fluid in a fixed domain $\Omega^f \subset \mathbb{R}^d$. The surrounding fluid is governed by the Navier-Stokes equations

$$\begin{cases} \rho^f (\partial_t \mathbf{u} + \mathbf{u} \cdot \nabla \mathbf{u}) - \operatorname{div} \sigma_f(\mathbf{u}, p) = \mathbf{0} & \text{in } \Omega^f, \\ \operatorname{div} \mathbf{u} = 0 & \text{in } \Omega^f. \end{cases} \quad (2)$$

Here, \mathbf{u} denotes the fluid velocity and p the fluid pressure in Ω^f . The Cauchy stress tensor is given by

$$\sigma_f := 2\mu_f \varepsilon(\mathbf{u}) - p\mathbf{I}, \quad \varepsilon(\mathbf{u}) = \frac{1}{2} (\nabla \mathbf{u} + \nabla \mathbf{u}^T),$$

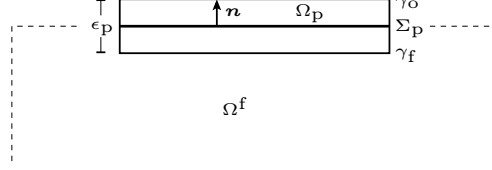


Figure 2: Porous medium domain Ω_p with interface γ_f to Ω^f and exterior boundary γ_o .

where \mathbf{I} denotes the identity matrix.

In the porous domain Ω_p , we assume a Darcy law

$$\begin{cases} \mathbf{u}_1 + \mathbf{K} \nabla p_1 = 0 & \text{in } \Omega_p, \\ \nabla \cdot \mathbf{u}_1 = 0 & \text{in } \Omega_p, \end{cases} \quad (3)$$

where \mathbf{u}_1 denotes the Darcy velocity, p_1 the Darcy pressure and \mathbf{K} is a $d \times d$ matrix such that the following decomposition holds

$$\mathbf{K} \nabla p_1 = K_\tau \nabla_\tau p_1 + K_n \partial_n p_1,$$

with $K_\tau, K_n \in \mathbb{R}^+$. Here, \mathbf{n} is the unit normal vector of the mid-surface Σ_p that points towards the exterior boundary γ_o , $\partial_n = \mathbf{n} \partial_n$ and $\nabla_\tau := P_\tau \nabla$ stands for the corresponding tangential part of the gradient

$$P_\tau := (\mathbf{I} - \mathbf{n} \otimes \mathbf{n}).$$

Furthermore, we assume that the porous layer is very thin and consider the limit case $\epsilon_p \rightarrow 0$. Let the outer boundary of Ω_p be denoted by γ_o and the interior boundary connecting to the fluid domain Ω^f by γ_f , see Figure 2. We assume zero normal velocity ($\mathbf{u}_1 \cdot \mathbf{n} = 0$) on the outer boundary γ_o and continuity of normal velocities and normal stresses on γ_f . For the tangential fluid stresses, we consider the Beavers-Joseph-Saffman coupling conditions [Saffman, 1971]. By $\mathbf{u}_\tau := P_\tau \mathbf{u}$, we denote the tangential part of the velocity vector and by $\sigma_{f,n} = \mathbf{n}^T \boldsymbol{\sigma}_f \mathbf{n}$ and $\sigma_{f,\tau} = P_\tau \boldsymbol{\sigma}_f \mathbf{n}$ the normal and tangential part of the Cauchy stress tensor $\boldsymbol{\sigma}_f$ introduced above. The coupling conditions between porous medium Ω_p and fluid Ω^f read

$$\begin{cases} \sigma_{f,n} = -p_1 & \text{on } \gamma_f, \\ \mathbf{u} \cdot \mathbf{n} = \mathbf{u}_1 \cdot \mathbf{n} & \text{on } \gamma_f, \\ \sigma_{f,\tau} = -\frac{\alpha}{\sqrt{K_\tau \epsilon_p}} \mathbf{u}_\tau & \text{on } \gamma_f. \end{cases} \quad (4)$$

We note that the condition for the tangential stresses, in the last line, corresponds to a Navier-slip boundary condition for the fluid. In contrast to this boundary condition for the fluid, the normal velocity $\mathbf{u} \cdot \mathbf{n}$ is not zero here, as the fluid can enter the porous layer.

The appropriate choice of the parameter α in the last line of (4) depends on the application. In the case that γ_f corresponds to a symmetry boundary within a larger fluid domain, where contact can take place, for example between two contacting valves, it is appropriate to set $\alpha = 0$ (pure slip). If the porous layer is, however, placed at a rigid wall, the Beavers-Joseph-Saffman condition with $\alpha > 0$ is more appropriate [Saffman, 1971, Mikelić and Jäger, 2000]. The parameter α depends on the structure of the porous layer. Values $0.01 < \alpha < 5$ have been suggested in [Nield et al., 2006]. We will consider both kind of conditions in the numerical examples of Section 4.

Introducing the averaged porous pressure P_1 as

$$P_1 = \frac{1}{2} (p_1|_{\gamma_f} + p_1|_{\gamma_o}) \quad \text{in } \Sigma_p, \quad (5)$$

the following equations can be derived in the limit case $\epsilon_p \rightarrow 0$ (see [Martin et al., 2005, Burman et al., 2021])

$$\begin{cases} -\nabla_\tau \cdot (\epsilon_p K_\tau \nabla_\tau P_1) = \mathbf{u} \cdot \mathbf{n} & \text{on } \Sigma_p, \\ \sigma_{f,n} = -P_1 - \frac{\epsilon_p K_n^{-1}}{4} \mathbf{u} \cdot \mathbf{n} & \text{on } \Sigma_p, \\ \sigma_{f,\tau} = -\frac{\alpha}{\sqrt{K_\tau \epsilon_p}} \mathbf{u}_\tau & \text{on } \Sigma_p. \end{cases} \quad (6)$$

Note that the only remaining porous medium variable is the averaged pressure P_1 . In the limit $K_n, K_\tau \rightarrow 0$, the coupling conditions turn into a Navier-slip boundary condition for the fluid on Σ_p .

2.3 Fluid-structure-porous-contact interaction model

We assume that $\Omega^f(t)$ is filled by an incompressible fluid governed by the Navier-Stokes equations. The domain $\Omega^s(t)$ is occupied by a solid media described by a beam or shell solid model (given in terms of an abstract surface differential operator \mathbf{L}) on a $(d-1)$ -dimensional domain Σ or by the elastodynamics equations in the case of a d -dimensional domain Ω^s . The fluid and solid equations are coupled with no-slip interface conditions on the fluid-structure interface $\Sigma(t)$. The solid is constrained to not penetrate into the porous medium Σ_p via the (relaxed) unilateral frictionless contact conditions

$$\mathbf{d} \cdot \mathbf{n} - g_\epsilon \leq 0, \quad \lambda \leq 0, \quad \lambda(\mathbf{d} \cdot \mathbf{n} - g_\epsilon) = 0 \quad \text{on } \Sigma, \quad (7)$$

Here, $g_\epsilon := g - \epsilon_g$, where g denotes the gap function to Σ_p and $\epsilon_g > 0$ is a small parameter. The symbol λ stands for the normal component of the contact traction, which corresponds to the Lagrange multiplier associated to the no-penetration condition.

The proposed fluid-structure-porous-contact interaction model is hence formulated as follows: Find the fluid velocity and pressure $\mathbf{u} : \Omega^f \times \mathbb{R}^+ \rightarrow \mathbb{R}^d$, $p : \Omega^f \times \mathbb{R}^+ \rightarrow \mathbb{R}$, the solid displacement and velocity $\mathbf{d} : \Omega^s \times \mathbb{R}^+ \rightarrow \mathbb{R}^d$, $\dot{\mathbf{d}} : \Omega^s \times \mathbb{R}^+ \rightarrow \mathbb{R}^d$, the Darcy porous pressure $P_1 : \Sigma_p \times \mathbb{R}^+ \rightarrow \mathbb{R}$ and the Lagrange multiplier $\lambda : \Sigma \times \mathbb{R}^+ \rightarrow \mathbb{R}$ such that, for all $t \in \mathbb{R}^+$, the following relations are satisfied

- Fluid problem:

$$\begin{cases} \rho^f(\partial_t \mathbf{u} + \mathbf{u} \cdot \nabla \mathbf{u}) - \operatorname{div} \boldsymbol{\sigma}_f(\mathbf{u}, p) = \mathbf{0} & \text{in } \Omega^f(t), \\ \operatorname{div} \mathbf{u} = 0 & \text{in } \Omega^f(t), \\ \mathbf{u} = \mathbf{0} & \text{on } \Gamma, \end{cases} \quad (8)$$

- Porous layer:

$$\begin{cases} -\nabla_\tau \cdot (\epsilon_p K_\tau \nabla_\tau P_1) = \mathbf{u}_1 \cdot \mathbf{n} & \text{on } \Sigma_p, \\ \epsilon_p K_\tau \tau \cdot \nabla_\tau P_1 = 0 & \text{on } \partial \Sigma_p, \end{cases} \quad (9)$$

- Solid problem:

$$\begin{cases} \rho^s \epsilon^s \partial_t \dot{\mathbf{d}} + \mathbf{L}(\mathbf{d}) = \mathbf{T} & \text{on } \Omega^s = \Sigma, \\ \dot{\mathbf{d}} = \partial_t \mathbf{d} & \text{on } \Omega^s = \Sigma, \\ \mathbf{d} = \mathbf{0} & \text{on } \partial \Omega^s \cap \Gamma, \end{cases} \quad (10)$$

in case of a thin-walled solid, or

$$\begin{cases} \rho^s \partial_t \dot{\mathbf{d}} - \operatorname{div} \boldsymbol{\sigma}_s(\mathbf{d}) = 0 & \text{on } \Omega^s, \\ \dot{\mathbf{d}} = \partial_t \mathbf{d} & \text{on } \Omega^s, \\ \mathbf{d} = \mathbf{0} & \text{on } \partial \Omega^s \cap \Gamma, \end{cases} \quad (11)$$

in case of a thick-walled solid.

- Contact conditions:

$$\mathbf{d} \cdot \mathbf{n} - g_\epsilon \leq 0, \quad \lambda \leq 0, \quad \lambda(\mathbf{d} \cdot \mathbf{n} - g_\epsilon) = 0 \quad \text{on } \Sigma. \quad (12)$$

- Fluid-structure coupling conditions:

$$\begin{cases} \boldsymbol{\phi} = \mathbf{I}_{\Omega^s} + \mathbf{d}, \quad \Omega_s(t) = \boldsymbol{\phi}_t(\Omega^s), \quad \Omega^f(t) = \Omega \setminus \Omega^s(t), \\ \mathbf{u} = \dot{\mathbf{d}} \circ \boldsymbol{\phi}_t^{-1} & \text{on } \Sigma(t), \end{cases} \quad (13)$$

and

$$\int_\Sigma (\mathbf{T} - \lambda \mathbf{n}) \cdot \mathbf{w} = - \int_{\Sigma(t)} [\boldsymbol{\sigma}_f(\mathbf{u}, p) \mathbf{n}] \cdot \mathbf{w} \circ \boldsymbol{\phi}_t^{-1}, \quad (14)$$

or

$$\int_\Sigma (\boldsymbol{\sigma}_s - \lambda \mathbf{I}) \mathbf{n} \cdot \mathbf{w} = - \int_{\Sigma(t)} \boldsymbol{\sigma}_f(\mathbf{u}, p) \mathbf{n} \cdot \mathbf{w} \circ \boldsymbol{\phi}_t^{-1} \quad (15)$$

for all test functions \mathbf{w} , respectively in the case of the coupling with a thin- or thick-walled solid.

- Fluid-porous coupling conditions:

$$\left\{ \begin{array}{ll} \mathbf{u}_l \cdot \mathbf{n} = \mathbf{u} \cdot \mathbf{n} & \text{on } \Sigma_p, \\ \sigma_{f,n} = -P_l - \underbrace{\frac{\epsilon_p K_n^{-1}}{4} \mathbf{u} \cdot \mathbf{n}}_{=: \sigma_p} & \text{on } \Sigma_p, \\ \sigma_{f,\tau} = -\frac{\alpha}{\sqrt{K_\tau \epsilon_p}} u_\tau & \text{on } \Sigma_p. \end{array} \right. \quad (16)$$

The relations in (13)-(15) enforce the geometrical compatibility and the kinematic and the dynamic coupling at the interface between the fluid and the solid, respectively. It should be noted that the no-penetration condition in (12) is already imposed at an ϵ_g -distance to the porous layer Σ_p . This modeling simplification circumvents most of the numerical difficulties associated with the topological change in the fluid domain induced by the exact contact condition (i.e., with $\epsilon = 0$), such as switching between the contact and fluid-solid interfaces and presence of isolated small fluid regions (see [Ager et al., 2020]). Moreover, it also facilitates the explicit treatment of the geometric condition in the fluid-structure coupling (see Section 3).

2.3.1 Mechanical consistency

In the fluid-structure-porous-contact interaction model (8)-(16), a very thin fluid layer always remains between the solid and porous medium during contact. Owing to the relations (16), the behavior of the fluid confined in the contact layer is expected to be very close to the one of the porous fluid. Indeed, this is a consequence of the kinematic-dynamics relations (16)_{1,2}, which are enforced both during and in absence of contact. If a part of $\Sigma(t)$ is in contact with Σ_p according to (7), the value of $\sigma_{f,n}$ (resp. $\mathbf{u} \cdot \mathbf{n}$) on this part $\Sigma(t)$ will be close to σ_p (resp. $\mathbf{u}_l \cdot \mathbf{n}$) on the corresponding part of Σ_p . As a result, all the kinematic and dynamic relations acting on the solid during contact have a physical meaning, which guarantees the mechanical consistency of the proposed fluid-structure-contact interaction model.

More precisely, owing to (15), in the case of a thick-walled solid the Lagrange multiplier for the no-penetration condition will formally assume the form

$$\lambda = \underbrace{\sigma_{s,n} - \sigma_{f,n}}_{=: \llbracket \sigma_n \rrbracket} \approx \sigma_{s,n} - \sigma_p \circ \pi \quad \text{on } \Sigma,$$

where we write $\sigma_{s,n} := \mathbf{n}^T \boldsymbol{\sigma}_s \mathbf{n}$ for the solid normal traction and π denotes a (closest-point) projection from $\Sigma(t)$ to Σ_p . Both, the solid stresses $\sigma_{s,n}$ and the "porous stresses" σ_p have a physical meaning during solid-porous contact. Hence, this porous-contact approach gives a physical meaning to the stresses generated in the infinitesimal fluid layer, in contrast to the relaxed contact formulation in [Burman et al., 2020a], where the fluid stresses $\sigma_{f,n}$ did not allow for a direct physical interpretation. A similar argumentation holds true for the thin-walled solid case, where

$$\lambda = (\rho^s \epsilon^s \partial_t \dot{\mathbf{d}} + \mathbf{L}(\mathbf{d})) \cdot \mathbf{n} + \llbracket \sigma_{f,n} \rrbracket \approx (\rho^s \epsilon^s \partial_t \dot{\mathbf{d}} + \mathbf{L}(\mathbf{d})) \cdot \mathbf{n} + \sigma_p \circ \pi - \sigma_{f,n}|_2 \quad \text{on } \Sigma.$$

In the spirit of [Alart and Curnier, 1991], the Lagrange multiplier can further be eliminated, which in the case of a thick-walled solid results in the non-linear contact condition

$$\llbracket \sigma_n \rrbracket = -\gamma_C \underbrace{[\mathbf{d} \cdot \mathbf{n} - g_\epsilon - \gamma_C^{-1} \llbracket \sigma_n \rrbracket]}_{=: P_{\gamma_C}(\mathbf{d} \cdot \mathbf{n}, \llbracket \sigma_n \rrbracket)} \Big|_+ \quad \text{on } \Sigma, \quad (17)$$

for $\gamma_C > 0$. This can be embedded in an elegant way in the variational formulation using a Nitsche-based approach, see [Burman et al., 2020a] and Section 3. For a thin solid, a similar approach is possible, with the additional difficulty that the normal solid traction on the mid-surface is given in terms of the normal PDE residual $(\rho^s \epsilon^s \partial_t \dot{\mathbf{d}} + \mathbf{L}(\mathbf{d})) \cdot \mathbf{n}$, which is rarely available at the discrete level. On the other hand, it has been shown (see [Burman et al., 2017, Scholz, 1984, Chouly and Hild, 2012]) for the case of a thin-walled solid that a pure penalty approach (i.e. neglecting the normal traction λ in the term P_{γ_C}) leads to a first-order approximation. The detailed variational formulations for both the case of a thick- and a thin-walled solid will be given in the next section.

The main advantage of this method is its simplicity. Moreover, it is expected from a mechanical point of view that the behavior of the fluid confined in the contact layer is close to the porous fluid, as

explained above. The porous medium and the structure are always coupled with the fluid only and never directly to each other. This avoids switches in the variational formulation, which would be necessary in the transition between fluid-solid and solid-porous interaction ([Burman et al., 2021]). On the other hand, the solid perceives indirectly the presence of the porous layer through the fluid stresses and velocity during contact. The resulting numerical approach is highly competitive in terms of computational costs compared to approaches using Lagrange multipliers and/or active-sets.

2.3.2 Seepage

The proposed fluid-structure-porous-contact interaction model (8)-(16) allows for seepage in the sense that fluid can flow through the porous layer Σ_p , for example to connect a cavity in the central part of the contact surface with the exterior fluid. These could emerge when the impact of the structure happens in the lateral parts of the structure first or when contact of the solid is released in a central part of the contact surface only. This is an important aspect in the modelling of fluid-structure-contact interaction, as otherwise unphysical configurations might result. As an example consider the situation sketched in Figure 3, where a solid body is in contact with the lower wall Σ_p at initial time (left sketch). When a (sufficiently strong) force \mathbf{f} is applied in the central part of Ω^s , while the body is fixed at the lateral parts, contact will be released in the central part only. If no seepage along Σ_p is allowed, a vacuum would emerge between Ω^s and Σ_p . While one could argue that this paradox is already circumvented by using the relaxed contact conditions (7), we note that only the porous layer gives a physical meaning to the fluid filling the contact layer.

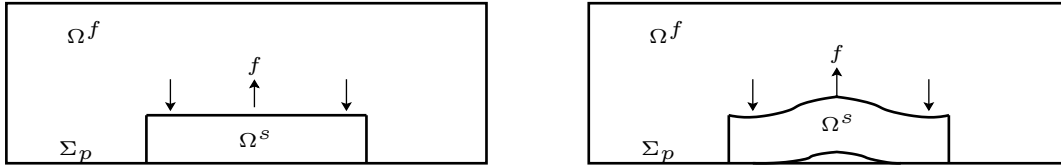


Figure 3: Illustrative example to motivate the role of seepage in fluid-structure interaction with contact: Contact of a solid body with the lower wall is released in the central part of the contact surface, when a specific force f is applied. Without seepage on Σ_p a vacuum would be created.

3 Numerical methods

This section is devoted to the numerical discretisation of the fluid-structure-porous-contact interaction model (8)-(16). Two numerical approaches will be considered which basically depend on thin- or thick-walled nature of the solid model and on the formalism used for the fluid-structure coupling (mixed Lagrangian-Eulerian or fully Eulerian formalisms). For an accurate discretisation of the fluid-structure-porous-contact interaction model (8)-(16), two different strategies will be considered in the numerical examples reported in Section 4. The first strategy is based on an unfitted Nitsche-XFEM method, drawing on [Burman and Fernández, 2014, Alauzet et al., 2016]. The second strategy is a fitted finite element method, following [Frei and Richter, 2014]. In both cases, we will use equal-order finite element methods.

To fix ideas, we will present the numerical approaches for two specific combinations of these components (mixed Lagrangian-Eulerian vs. Fully Eulerian, fitted vs. unfitted finite elements, thick-walled vs. thin-walled structures), namely a mixed Lagrangian-Eulerian approach with a thin-walled solid using unfitted finite elements in Section 3.1 and a fully Eulerian approach with a thick-walled solid using fitted finite element discretisation in Section 3.2. Different combinations are possible as well, but will not be considered in the remainder of this article.

3.1 Lagrange-Eulerian formalism with immersed thin-walled solids

In what follows, the parameter $\delta t > 0$ stands for the time-step length and $t_n := n\delta t$ denotes the time instant at time level $n \in \mathbb{N}$. The symbol x^n generally denotes an approximation of $x(t_n)$, for a given time valued function $x(t)$. We also introduced the notation

$$\partial_{\delta t} x^n := \frac{1}{\delta t} (x^n - x^{n-1}),$$

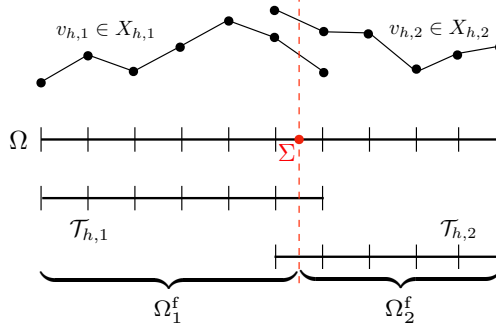


Figure 4: One dimensional illustration of the overlapping meshes $\mathcal{T}_{h,i}^n$ and of the construction of the discrete spaces $X_{h,i}^n$.

for the first-order backward difference.

We consider the fluid-structure-porous-contact interaction problem (8)-(16) in the case of the coupling with immersed thin-walled solids. The time discretisation is performed with a backward-Euler scheme, including a semi-implicit treatment of the convective term in (8) and an explicit treatment of the geometric coupling (13)₁. As regards the spatial discretisation, an unfitted finite element approximation with overlapping meshes is considered for the fluid-solid coupling, by drawing on the Nitsche-XFEM method reported in [Alauzet et al., 2016, Burman and Fernández, 2014]. The fluid-porous system is discretised by a standard fitted finite element approximation.

For the solid, we start by assuming that there exists a positive form $a^s : \mathbf{W} \times \mathbf{W} \rightarrow \mathbb{R}$, linear with respect to the second argument, such that

$$a^s(\mathbf{d}, \mathbf{w}) = (\mathbf{L}(\mathbf{d}), \mathbf{w})_\Sigma$$

for all $\mathbf{w} \in \mathbf{W} := [H_{\Gamma \cap \partial \Sigma}^1(\Sigma)]^d$, where \mathbf{W} stands for the space of admissible displacements. Let $\{\mathcal{T}_h^s\}_{0 < h < 1}$ be a family of triangulations of Σ . We consider the standard space of continuous piecewise affine functions

$$X_h^s := \{v_h \in C^0(\bar{\Sigma}) \mid v_h|_K \in \mathbb{P}_1(K), \quad \forall K \in \mathcal{T}_h^s\}, \quad \mathbf{W}_h := [X_h^s]^d \cap \mathbf{W}.$$

The contact condition (12) is approximated via a penalty method (see, e.g., [Scholz, 1984]), by adding the following penalty term into the solid discrete problem:

$$\frac{\gamma_c E \epsilon^s}{h^2} ([\mathbf{d}_h^n \cdot \mathbf{n} - g_\varepsilon]_+, \mathbf{w}_h)_\Sigma,$$

where E is the solid Young modulus and $\gamma_c > 0$ is the (dimensionless) penalty parameter.

For a given discrete displacement approximation $\mathbf{d}_h^n \in \mathbf{W}_h$ at time t_n , we define its associated deformation map by $\phi_h^n := \mathbf{I}_\Sigma + \mathbf{d}_h^n$. This map characterises the current solid configuration (i.e., at time level n), as $\Sigma^n := \phi_h^n(\Sigma)$. As indicated above, we consider an explicit update for the physical fluid domain in (13)₁, namely,

$$\Omega^{f,n} := \Omega \setminus \Sigma^{n-1}, \quad (18)$$

which has the effect of removing the geometrical non-linearities in the fluid problem (8).

Let $\{\mathcal{T}_h\}_{0 < h < 1}$ a family of triangulations of Ω . Owing to (18), for each \mathcal{T}_h we defined two overlapping meshes $\mathcal{T}_{h,i}^n$, $i = 1, 2$, such that $\mathcal{T}_{h,i}^n$ covers the i -th fluid region $\Omega_i^{f,n}$ defined by Σ^{n-1} through (18). Note that each triangulation $\mathcal{T}_{h,i}^n$ is fitted to the exterior boundary $\Gamma \cup \Sigma_p$, but in general not to Σ^{n-1} (nor \mathcal{T}_h^s), see Figure 4. There will be duplicated elements, i.e., such that $K \in \mathcal{T}_{h,1}^n \cap \mathcal{T}_{h,2}^n$, but this is only allowed when $K \cap \Sigma^{n-1} \neq \emptyset$. We denote by $\Omega_{h,i}^{f,n}$ the domain covered by $\mathcal{T}_{h,i}^n$, viz.,

$$\Omega_{h,i}^{f,n} := \text{int} \left(\bigcup_{K \in \mathcal{T}_{h,i}^n} K \right).$$

We can hence introduce the following spaces of continuous piecewise affine functions

$$X_{h,i}^n := \left\{ v_h \in C^0(\bar{\Omega}_{h,i}^{f,n}) \mid v_h|_K \in \mathbb{P}_1(K), \quad \forall K \in \mathcal{T}_{h,i}^n \right\}.$$

and set

$$\mathbf{V}_{h,i}^n := [X_{h,i}^n]^d \cap [H_\Gamma^1(\Omega^{f,n})]^d, \quad Q_{h,i}^n := X_{h,i}^n \cap L_0^2(\Omega^{f,n}).$$

For the approximation of the fluid velocity and pressure we will consider the following time-dependent discrete product spaces

$$\mathbf{V}_h^n := \mathbf{V}_{h,1}^n \times \mathbf{V}_{h,2}^n, \quad Q_h^n := Q_{h,1}^n \times Q_{h,2}^n. \quad (19)$$

The functions in (19) are continuous in the physical fluid domain $\Omega_i^{f,n}$, but discontinuous across the interface location Σ^{n-1} (see Figure 4).

Algorithm 1 Strongly coupled scheme for fluid-structure-porous-contact interaction (thin-walled solid).

For $n \geq 1$:

1. Interface update:

$$\phi_h^{n-1} = \mathbf{I}_\Sigma + \mathbf{d}_h^{n-1}, \quad \Sigma^{n-1} = \phi_h^{n-1}(\Sigma), \quad \Omega^{f,n} = \Omega \setminus \Sigma^{n-1}.$$

2. Find $(\mathbf{u}_h^n, p_h^n, \dot{\mathbf{d}}_h^n, \mathbf{d}_h^n, P_{1,h}^n) \in \mathbf{V}_h^n \times Q_h^n \times \mathbf{W}_h \times \mathbf{W}_h \times \mathbf{S}_h$ with $\dot{\mathbf{d}}_h^n = \partial_{\delta t} \mathbf{d}_h^n$ such that

$$\begin{aligned} & \rho^f (\partial_{\delta t} \mathbf{u}_h^n, \mathbf{v}_h)_{\Omega^n} + a_h^{f,n}(\mathbf{u}_h^{n-1}; (\mathbf{u}_h^n, p_h^n), (\mathbf{v}_h, q_h)) + \rho^s \epsilon^s (\partial_{\delta t} \dot{\mathbf{d}}_h^n, \mathbf{w}_h)_\Sigma + a^s(\mathbf{d}_h^n, \mathbf{w}_h) \\ & + \frac{\gamma_c E \epsilon^s}{h^2} ([\mathbf{d}_h^n \cdot \mathbf{n} - g_\epsilon]_+, \mathbf{w}_h \cdot \mathbf{n})_\Sigma - \sum_{i=1}^2 (\sigma_f(\mathbf{u}_{h,i}^n, p_{h,i}^n) \mathbf{n}_i, \mathbf{v}_{h,i} - \mathbf{w}_h)_{\Sigma^{n-1}} \\ & - \sum_{i=1}^2 (\mathbf{u}_{h,i}^n - \dot{\mathbf{d}}_h^n, \sigma_f(\mathbf{v}_{h,i}, -q_{h,i})) \mathbf{n}_i)_{\Sigma^{n-1}} + \frac{\gamma \mu}{h} \sum_{i=1}^2 (\mathbf{u}_{h,i}^n - \dot{\mathbf{d}}_h^n, \mathbf{v}_{h,i} - \mathbf{w}_h)_{\Sigma^{n-1}} \\ & + \frac{\alpha}{\sqrt{K_\tau \epsilon_p}} (\mathbf{u}_{h,\tau}^n, \mathbf{v}_{h,\tau})_{\Sigma_p} - (\sigma_p, \mathbf{v}_h \cdot \mathbf{n})_{\Sigma_p} + (\epsilon_p K_\tau \nabla_\tau P_{1,h}^n, \nabla_\tau q_{1,h})_{\Sigma_p} - (\mathbf{u}_h^n \cdot \mathbf{n}, q_{1,h})_{\Sigma_p} = 0 \end{aligned} \quad (20)$$

for all $(\mathbf{v}_h, q_h, \mathbf{w}_h, q_{1,h}) \in \mathbf{V}_h^n \times Q_h^n \times \mathbf{W}_h \times \mathbf{S}_h$, where the porous stress σ_p is given by

$$\sigma_p := -P_{1,h}^n - \frac{\epsilon_p K_n^{-1}}{4} \mathbf{u}_h^n \cdot \mathbf{n} \quad \text{on } \Sigma_p.$$

We can now introduce the corresponding fluid discrete tri-linear form (see [Alauzet et al., 2016]):

$$\begin{aligned} a_h^{f,n}(\mathbf{z}_h; (\mathbf{u}_h, p_h), (\mathbf{v}_h, q_h)) &:= 2\mu (\epsilon(\mathbf{u}_h), \epsilon(\mathbf{v}_h))_{\Omega^{f,n}} + \rho^f (\mathbf{z}_h \cdot \nabla \mathbf{u}_h, \mathbf{v}_h)_{\Omega^{f,n}} + \frac{\rho^f}{2} ((\operatorname{div} \mathbf{z}_h) \mathbf{u}_h, \mathbf{v}_h)_{\Omega^{f,n}} \\ & - \rho^f (\{\mathbf{z}_h\} \cdot \mathbf{n} \llbracket \mathbf{u}_h \rrbracket, \{\mathbf{v}_h\})_{\Sigma^{n-1}} - \frac{\rho^f}{2} (\llbracket \mathbf{z}_h \cdot \mathbf{n} \rrbracket, \{\mathbf{u}_h \cdot \mathbf{v}_h\})_{\Sigma^{n-1}} \\ & - (p_h, \operatorname{div} \mathbf{v}_h)_{\Omega^{f,n}} + (\operatorname{div} \mathbf{u}_h, q_h)_{\Omega^{f,n}} \\ & + s_{v,h}^n(\mathbf{z}_h; \mathbf{u}_h, \mathbf{v}_h) + s_{p,h}^n(\mathbf{z}_h; p_h, q_h) + g_h^n(\mathbf{u}_h, \mathbf{v}_h). \end{aligned}$$

For consistency the bulk terms are integrated in the physical domain $\Omega^{f,n}$, which requires a specific track of the interface intersections within the fluid domain (see e.g. [Massing et al., 2013, Alauzet et al., 2015, Zonca et al., 2018]). The terms $s_{v,h}^n$ and $s_{p,h}^n$ respectively correspond to the continuous interior penalty velocity and pressure stabilisation operators, given by (see, e.g., [Burman et al., 2006]):

$$\begin{aligned} s_{v,h}^n(\mathbf{z}_h; \mathbf{u}_h, \mathbf{v}_h) &:= \gamma_v h^2 \sum_{i=1}^2 \sum_{F \in \mathcal{F}_{h,i}^n} \xi(\operatorname{Re}_F(\mathbf{z}_h)) \|\mathbf{z}_h \cdot \mathbf{n}\|_{L^\infty(F)} (\llbracket \nabla \mathbf{u}_h \rrbracket_F, \llbracket \nabla \mathbf{v}_h \rrbracket_F)_F, \\ s_{p,h}^n(\mathbf{z}_h; p_h, q_h) &:= \gamma_p h^2 \sum_{i=1}^2 \sum_{F \in \mathcal{F}_{h,i}^n} \frac{\xi(\operatorname{Re}_F(\mathbf{z}_h))}{\|\mathbf{z}_h\|_{L^\infty(F)}} (\llbracket \nabla p_h \rrbracket_F, \llbracket \nabla q_h \rrbracket_F)_F, \end{aligned}$$

where $\mathcal{F}_{h,i}^n$ denotes the set of interior edges or faces of $\mathcal{T}_{h,i}^n$, $\operatorname{Re}_F(\mathbf{z}_h) := \rho^f \|\mathbf{z}_h\|_{L^\infty(F)} h \mu^{-1}$ denotes the local Reynolds number, $\xi(x) := \min\{1, x\}$ is a cut-off function and $\gamma_p, \gamma_v > 0$ are user-defined parameters.

Finally, g_h^n is the so-called ghost-penalty operator, given by

$$g_h^n(\mathbf{u}_h, \mathbf{v}_h) := \gamma_g \mu h \sum_{i=1}^2 \sum_{F \in \mathcal{F}_{i,h}^{\Sigma^{n-1}}} (\llbracket \nabla \mathbf{u}_{i,h} \rrbracket_F, \llbracket \nabla \mathbf{v}_{i,h} \rrbracket_F)_F,$$

where $\mathcal{F}_{i,h}^{\Sigma^{n-1}}$ denotes the set of interior edges or faces of the elements intersected by Σ^{n-1} . This term is added to guarantee robustness independent of the way the interface cuts the fluid mesh. The underlying idea is to extend the coercivity of the bi-linear form to the whole computational domain, see [Burman, 2010] or [Lehrenfeld and Olshanskii, 2019] for different possibilities.

For the approximation of the porous system, we consider a family of triangulation $\{\mathcal{T}_h^p\}_{h>0}$ of Σ_p , so that each \mathcal{T}_h^p is fitted \mathcal{T}_h . We then consider the standard space of continuous piecewise affine functions for the approximation of the porous pressure P

$$\mathbf{S}_h := \{v_h \in C^0(\overline{\Sigma_p}) \mid v_h|_K \in \mathbb{P}_1(K), \quad \forall K \in \mathcal{T}_h^p\}.$$

In summary, the resulting fully discrete method is reported in Algorithm 1. We use the notation $\mathbf{u}_{h,i}^n, \mathbf{v}_{h,i}^n, p_{h,i}^n, q_{h,i}^n$ ($i = 1, 2$) introduced in (1) for the two parts of the discontinuous functions across Σ^{n-1} . Note that the kinematic-dynamic interface coupling (13)₂-(14) is enforced in a consistent and strongly coupled fashion through Nitsche's method (see [Burman and Fernández, 2014, Alauzet et al., 2016]).

Remark 3.1. *If the interface has a boundary inside the fluid domain (the so-called), we consider the construction of the fluid and solid discrete spaces proposed in [Alauzet et al., 2016] (see [Gerosa, 2021, Chapter 6] for an extension to the 3D case). A virtual interface $\tilde{\Sigma}^{n-1}$ is introduced by connecting the interface tip with the fluid vertex opposite to the edge intersected by the interface and therefore the fluid domain is closed. Afterwards, we enforce the kinematic/dynamic continuity of the fluid on $\tilde{\Sigma}^{n-1}$ in a discontinuous Galerkin fashion (see, e.g., [Di Pietro and Ern, 2012]). More precisely, the following terms are added to (20)*

$$-(\llbracket \boldsymbol{\sigma}_i(\mathbf{u}_h^n, p_h^n) \rrbracket \mathbf{n}, \llbracket \mathbf{v}_h \rrbracket)_{\tilde{\Sigma}^{n-1}} - (\llbracket \boldsymbol{\sigma}_i(\mathbf{v}_h, -q_h) \rrbracket \mathbf{n}, \llbracket \mathbf{u}_h^n \rrbracket)_{\tilde{\Sigma}^{n-1}} + \frac{\gamma \mu}{h} (\llbracket \mathbf{u}_h^n \rrbracket, \llbracket \mathbf{v}_h \rrbracket)_{\tilde{\Sigma}^{n-1}}.$$

3.2 Fully Eulerian formalism with immersed thick-walled solids

In a fully Eulerian approach the current displacement $\mathbf{d}(\mathbf{x}, t)$ is defined by the relation

$$\mathbf{x} - \mathbf{d}(\mathbf{x}, t) = \hat{\mathbf{x}}, \quad (21)$$

where $\hat{\mathbf{x}}$ is the corresponding point in the reference configuration Ω^s . This means that the displacement can be used to trace back points $\mathbf{x} \in \Omega^s(t)$ to their reference position $\hat{\mathbf{x}}$ in Ω^s and hence to determine the domain affiliation of a point $\mathbf{x} \in \Omega$ at time t . As in the previous section, we use again an explicit approach to avoid the issues related to geometrical non-linearities

$$\Omega^{s,n} := \{\mathbf{x} \in \Omega, \mid \mathbf{x} - \mathbf{d}_h^{n-1} \in \Omega^s\}, \quad \Sigma^n := \{\mathbf{x} \in \Omega, \mid \mathbf{x} - \mathbf{d}_h^{n-1} \in \Sigma\}, \quad \Omega^{f,n} := \Omega \setminus (\Omega^{s,n} \cup \Sigma^n).$$

Numerically, the domain affiliations can be determined by the Initial Point Set (backward characteristics) method (see, e.g., [Dunne, 2006, Cottet et al., 2008, Frei, 2016]). To evaluate the displacement \mathbf{d}_h^{n-1} in points $\mathbf{x} \in \Omega^{f,n-1}$ near the interface Σ^{n-1} , that could belong to $\Omega^{s,n}$ in the next step, an extension of the solid displacement to a small layer around the interface is required (see, e.g., [Richter, 2013]). The domain affiliation can be computed in a separate step before setting up the variational formulation as shown in Algorithm 2, or "on-the-fly" while setting up the finite element formulation.

As an alternative to the unfitted finite element method presented in the previous section, we consider here a fitted finite element method for spatial discretisation. We briefly describe the locally modified finite element method as an example in two space dimensions (see [Frei and Richter, 2014]). The method is based on a fixed coarse triangulation \mathcal{T}_{2h} , which is independent of the interface position, and a further subtriangulation of the coarse elements $P \in \mathcal{T}_{2h}$, which resolves the interface, see Figure 5. We restrict ourselves to linear finite elements and a linear interface approximation. A second-order approximation has been presented recently in [Frei et al., 2020].

In order to resolve the interface locally, we split each coarse cell cut by the interface into 8 subtriangles K_1, \dots, K_8 and move some of the interior vertices to the interface, such that a linear interface

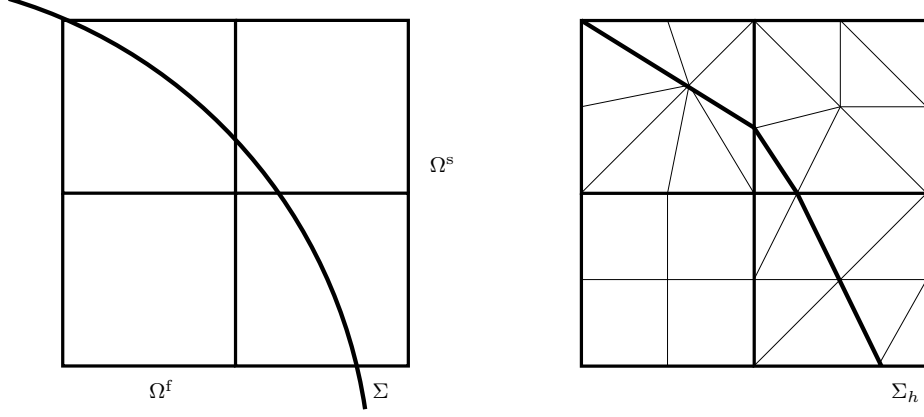


Figure 5: Example of a locally fitted finite element discretisation with 4 coarse cells.

approximation is obtained. The position of the 9 degrees of freedom x_1, \dots, x_9 in each coarse cell are described by a piecewise linear reference map from the reference patch $\hat{P} = [0, 1]^2$

$$\xi_P : \hat{P} \mapsto P, \quad \xi_P \in Q_P := \{\phi_h \in C^0(\hat{P}) \mid \xi|_{K_i} \in P_1(K_i), i = 1, \dots, 8\}$$

that fulfills the 9 conditions $\xi_P(\hat{x}_i) = x_i$, $i = 1, \dots, 9$, where \hat{x}_i denotes the (fixed) Lagrangian points on the reference patch. In elements that are not affected by the interface piecewise bilinear shape functions can be used on four quadrilaterals alternatively, see the lower left coarse cell in Figure 5. The locally modified finite element space is then given by

$$X_h^{\text{lmfem},n}(\Omega) := \{\phi_h \in C^0(\bar{\Omega}), \mid (\phi_h \circ \xi^{-1})|_P \in Q_P \forall P \in \mathcal{T}_{2h}\}.$$

By $X_h^{\text{lmfem},n}(\Omega^i)$ we denote the space that results by eliminating all degrees of freedom that do not lie in a subdomain $\Omega^i \subset \Omega$ or on its boundary. Then, we define the spaces

$$\mathbf{V}_h^n := [X_h^{\text{lmfem},n}(\Omega^{f,n}) \cap H_\Gamma^1(\Omega^{f,n})]^2, \quad Q_h^n := X_h^{\text{lmfem},n}(\Omega^{f,n}), \quad \mathbf{W}_h^n := [X_h^{\text{lmfem},n}(\Omega^{s,n}) \cap H_\Gamma^1(\Omega^{s,n})]^2.$$

The space S_h is defined as in Section 3.1. We use an implicit form of the fluid semi-linear form

$$\begin{aligned} a_h^{f,n}(\mathbf{u}_h, p_h; \mathbf{v}_h, q_h) := & 2\mu(\epsilon(\mathbf{u}_h), \epsilon(\mathbf{v}_h))_{\Omega^{f,n}} + \rho^f(\mathbf{u}_h \cdot \nabla \mathbf{u}_h, \mathbf{v}_h)_{\Omega^{f,n}} - (p_h, \text{div } \mathbf{v}_h)_{\Omega^{f,n}} \\ & + (\text{div } \mathbf{u}_h, q_h)_{\Omega^{f,n}} + s_{p,h}^n(\mathbf{z}_h; p_h, q_h). \end{aligned}$$

To cope with the lack of inf-sup-stability of the discrete spaces, we use the (anisotropic) CIP pressure stabilisation developed in [Frei, 2019] for $s_{p,h}^n$. In contrast to (3.1), we have omitted the convection stabilisation, which will not be needed in the examples with a thick solid below. Moreover, a ghost-penalty term is not required, as we use a fitted finite element discretisation.

For the solid, we assume a hyperelastic material law with a corresponding variational formulation of the form

$$a^{s,n}(\mathbf{d}_h, \mathbf{w}_h) := (\boldsymbol{\sigma}_s(\mathbf{d}_h), \nabla \mathbf{w}_h)_{\Omega^{s,n}},$$

where $\boldsymbol{\sigma}_s$ denotes the Cauchy stress tensor.

Concerning time discretisation let us first note that the variables \mathbf{u}_h^{n-1} and \mathbf{d}_h^{n-1} are undefined on parts of $\Omega^{s,n}$ and $\Omega^{f,n}$, respectively, as both Ω^s and Ω^f are time-dependent. Thus, the method of lines can not be applied in a straight-forward way. To deal with this issue, we use the dG(0) variant of a family of Galerkin schemes that incorporates the characteristics of the domain movement in the Galerkin spaces [Frei and Richter, 2017b]. For the dG(0) variant the difference to a standard backward Euler scheme lies solely in the discretisation of the time derivative. We introduce the notation

$$\tilde{\partial}_{\delta t} \mathbf{u}_h^n = \frac{\mathbf{u}_h^n - (\mathbf{u}_h^{n-1} \circ \Psi)}{\delta t} - \partial_t \Psi \cdot \nabla \mathbf{u}_h^n,$$

where Ψ is an (arbitrary) map defined in Ω that maps $\Omega^{f,n}$ to $\Omega^{f,n-1}$ and $\Omega^{s,n}$ to $\Omega^{s,n-1}$, respectively. Alternatively, one could use Eulerian time-stepping schemes with suitable extension operators. An implicit

Algorithm 2 Strongly coupled Eulerian approach for an FSI-contact problem with a thick-walled solid.

For $n \geq 1$:

1. Update the domain affiliations

$$\Omega^{s,n} := \{x \in \Omega, |x - d_h^{n-1} \in \Omega^s\}, \quad \Sigma^n := \{x \in \Omega, |x - d_h^{n-1} \in \Sigma\}, \quad \Omega^{f,n} := \Omega \setminus (\Omega^{s,n} \cup \Sigma^n).$$

2. Find $(u_h^n, p_h^n, d_h^n, P_{1,h}^n) \in V_h^n \times Q_h^n \times W_h^n \times W_h^n \times S_h$ with $\dot{d}_h^n = \tilde{\partial}_{\delta t} d_h^n$ and

$$\begin{aligned} & \rho^f(\tilde{\partial}_{\delta t} u_h^n, v_h)_{\Omega^{f,n}} + a_h^{f,n}(u_h^n, p_h^n; v_h, q_h) + \rho^s(\tilde{\partial}_{\delta t} d_h^n, w_h)_{\Omega^{s,n}} + a^{s,n}(d_h^n, w_h) \\ & + \frac{\gamma_c E}{h}([\tilde{P}_{\gamma_c}(d_h^n)]_+, w_h \cdot n)_{\Sigma^n} - (\sigma_f(u_h^n, p_h^n) n, v_h - w_h)_{\Sigma^n} \\ & - (u_h^n - d_h^n, \sigma_f(v_h, -q_h) n)_{\Sigma^n} + \frac{\gamma \mu}{h}(u_h^n - d_h^n, v_h - w_h)_{\Sigma^n} \\ & + \frac{\alpha}{\sqrt{K_\tau \epsilon_p}}(u_{\tau,h}^n, v_{h,\tau})_{\Sigma_p} - (\sigma_p, v_h \cdot n)_{\Sigma_p} + (\epsilon_p K_\tau \nabla_\tau P_{1,h}^n, \nabla_\tau q_{1,h})_{\Sigma_p} - (u_{h,n}^n, q_{1,h})_{\Sigma_p} = 0 \end{aligned} \quad (22)$$

for all $(v_h, q_h, w_h, q_{1,h}) \in V_h^n \times Q_h^n \times W_h^n \times S_h$, with the porous stress σ_p as defined in Algorithm 1 and the contact term \tilde{P}_{γ_c} defined in (23).

extension my means of ghost-penalties has been studied in [Lehrenfeld and Olshanskii, 2019, Burman et al., 2020b].

Finally, let us note that due to the different meaning of the displacement d_h^n in the current frame $\Omega^{s,n}$ (see (21)), the no-penetration condition in (12) becomes

$$d_h^n - (d_h^{n-1} \circ \Psi) - \tilde{g}_\epsilon^n \leq 0$$

where \tilde{g}_ϵ^n denotes the current distance to the lower wall Σ_p minus ϵ and Ψ is a map from Σ^n to Σ^{n-1} . The contact term takes the form

$$\tilde{P}_{\gamma_c}(d_h^n) = d_h^n - (d_h^{n-1} \circ \Psi) - \tilde{g}_\epsilon^n - \gamma_C^{-1} \llbracket \sigma_n \rrbracket, \quad (23)$$

where $\gamma_C = \frac{\gamma_c E}{h}$, E denotes the elasticity modulus of the solid and γ_c is a (dimensionless) contact parameter. We note that in contrast to the $\mathcal{O}(h^{-2})$ -weighting in the thin case, a weighting of $\mathcal{O}(h^{-1})$ is needed here [Chouly and Hild, 2012]. The resulting numerical method is reported in Algorithm 2.

Remark 3.2. (Stability) In [Burman et al., 2020a] a stability result has been derived for a very similar variational formulation with slip- or no-slip boundary conditions on Σ_p instead of the porous medium. An analogous result can easily be shown for both the variational formulations in (20) and (22) using the same technique.

4 Numerical experiments

In this section, we present different numerical examples to investigate the properties and the capabilities of the numerical approaches. First, we investigate the fluid-porous coupling by considering two disconnected fluid reservoirs that are connected through a thin-walled porous media in Section 4.1. Then, we investigate the full fluid-structure-porous-contact problem for a thin-walled solid by means of a deflected thin elastic valve in Section 4.2. As introduced in Section 3.1, we use an unfitted discretisation and solve the solid equations on the reference domain $\Omega^s = \Sigma$. Finally, we investigate the case of a thick solid in Section 4.3, namely an elastic ball that falls down and bounces within a viscous fluid. Here, a Fully Eulerian approach is used in combination with the locally fitted finite element method, as described in Section 3.2.

4.1 Reservoirs connected via porous layer

In this example, we consider two disconnected fluid reservoirs, connected through a thin-walled porous interface located on the bottom wall Σ_p , as shown in Figure 6. The fluid domain Ω^f is shown in Figure 6 and Σ_p is a segment with extremities $(0, 0)$ and $(2, 0)$.

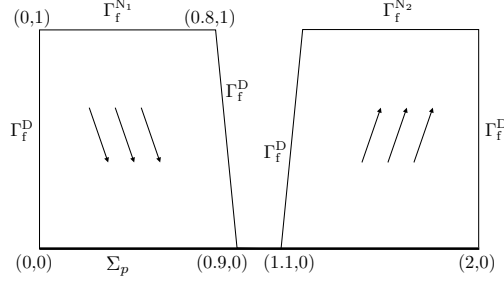


Figure 6: Geometrical configuration for the Stokes model with a thin-walled porous medium on the bottom wall.

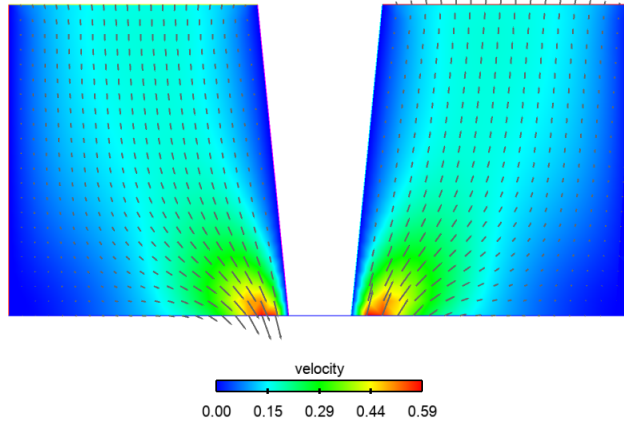


Figure 7: Snapshot of the fluid velocity at time $t = 0.25$.

Regarding the fluid boundary conditions, we impose a pressure drop across the two parts of the top boundary. A traction is imposed on Γ_f^{N1} in terms of a sinusoidal time-dependent pressure $p_{in}(t)$, namely,

$$p_{in}(t) = 5 \cdot \sin(2\pi t), \quad \forall t \in \mathbb{R}^+,$$

while a zero traction is enforced on Γ_f^{N2} . Additionally, a no-slip boundary condition is enforced on Γ_f^D . The considered physical parameters are $\mu = 0.03$, $\rho^f = 1$, $\varepsilon_p = 0.01$ and $K_\tau = K_n = 1$. We consider an approximation of the Beavers-Joseph-Saffmann condition for the tangential stresses, in which we let $\alpha = 0$.

The purpose of this example is to illustrate how the porous model is able to connect the fluid flow between the two containers. This can be clearly inferred from the results reported in Figure 7 and Figure 8 at $t = 0.25$, which, respectively, show a snapshot of the fluid velocity, the elevation of the fluid pressure and the associated porous pressure. As we can see, the fluid is entering into the porous layer from the left reservoir and leaving the porous interface into the right one.

4.2 Idealised valve with contact

In this test, we consider a full FSI-contact problem with a thin-walled solid. This numerical example corresponds to the idealised valve test with possible contact on the porous layer Σ_p . The geometry is shown in Figure 9(a). The computational domain is a rectangle $\Omega = [0, 8] \times [0, 0.805]$, where the upper boundary is a symmetry axis (we imagine a second symmetrical valve on top), which means that we impose the "slip" condition $\sigma_{f,\tau} = 0$ in (9), letting $\alpha = 0$. As reference configuration for the solid, Σ , we consider a curve segment with end points $A = (4, 0)$ and $B = (5.112, 0.483)$, parametrised by the analytical function

$$y(x) = \frac{1}{2} \sqrt{1 - \frac{(x - 11/2)^2}{(3/2)^2}}, \quad x \in [4, 5.112].$$

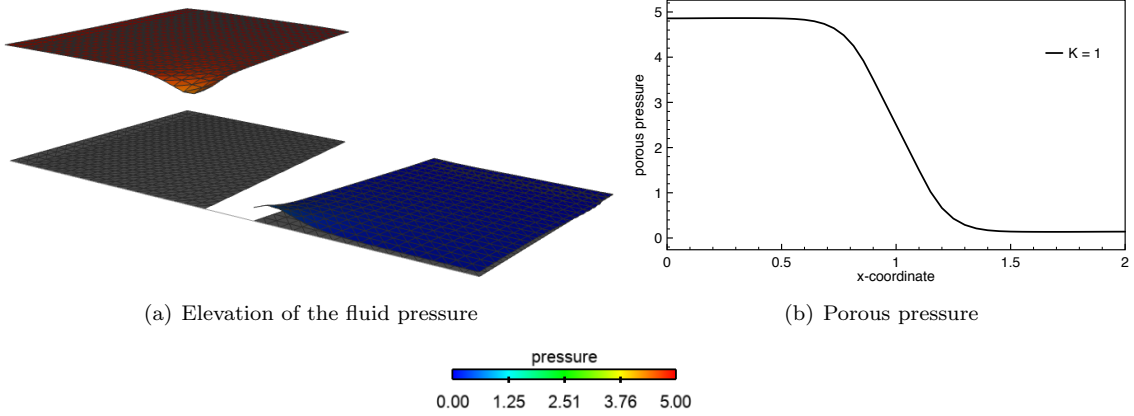


Figure 8: Fluid and porous pressures at $t = 0.25$.

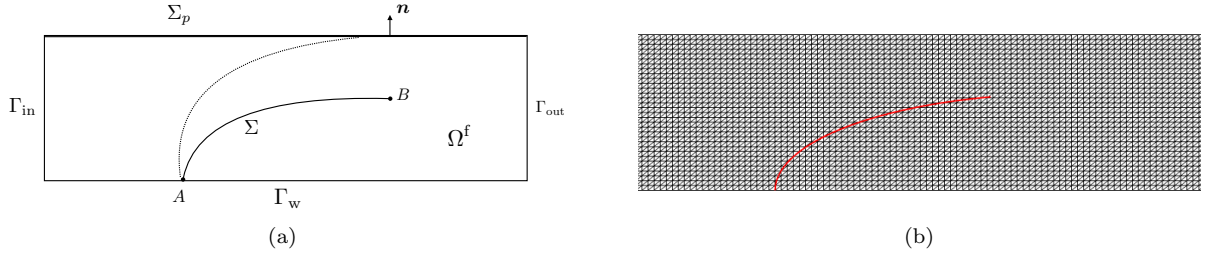


Figure 9: (a) Geometric configuration of the idealised valve with contact, (b) Zoom of the leaflet mesh and fluid mesh.

All the following units are given in the CGS units system. The physical parameters used for the fluid in this test are $\rho^f = 1$, $\mu = 0.03$. For the solid we have $\rho^s = 1.2$, $\epsilon^s = 0.065$, the Young's modulus $E = 10^7$ and the Poisson's ratio $\nu = 0.4$. Regarding the porous medium, we consider $\epsilon_p = 0.01$ and we explore the influence of the porous layer on the contact dynamics by changing the hydraulic conductivity parameters $K_\tau = K_n = \{10^{-i}\}_{i=1}^3$ and by comparing it with the situation of a simple wall on Σ_p , where we enforce a symmetry condition.

Regarding the boundary condition, a no-slip condition is enforced on the lower boundary Γ_w , zero traction on the outflow boundary Γ_{out} and a traction condition on Γ_{in} , in terms of the following time-dependent pressure:

$$p_{in}(t) = \begin{cases} -200 \operatorname{atanh}(100t) & \text{if } 0 < t < 0.7, \\ 200 & \text{if } t \geq 0.7. \end{cases}$$

The final time is $T = 1$, which corresponds to one full valve oscillation cycle. The fluid and the solid are initially at rest and the beam is pinched at the bottom tip A . In this test, the solid is described by a non-linear Reissner–Mindlin curved beam model with a MITC spacial discretisation. The ghost penalty parameter has been set to $\gamma_g = 1$ and the CIP stabilisation parameters to $\gamma_v = \gamma_p = 10^{-2}$. In this particular test case, the gap function is defined as the initial distance of a point on Σ to the wall Σ_p in the direction of \mathbf{n}_1 , namely $g = y_{\Sigma_p} - y(x)$. The contact parameters are given by $\epsilon_g = 0.01$ and $\gamma_c = 5 \cdot 10^{-3}$ as in [Boilevin-Kayl et al., 2019]. The relaxation parameter ϵ_g is chosen in such a way that the generated artificial gap is below h , typically $\epsilon_h \approx h/2$. The penalty parameter γ_c (independent of h) is chosen to avoid penetration (i.e., not very small) and in such a way that the term (17) does not perturb the convergence of the Newton solver in the solid (the operator $[\cdot]_+$ is not differentiable at 0).

The fluid mesh has 16384 triangles and the solid mesh 50 edges. We have $h \approx 0.04$. The zoom on both meshes is presented in Figure 9(b). The time discretisation parameter is $\delta t = 10^{-3}$ and the Nitsche parameter is set to $\gamma = 100$.

Let us first consider a test case with $K = K_\tau = K_n = 10^{-3}$. We report in Figure 10 the velocity magnitude at two different instants. In Figure 10(a) we report the approximation obtained at time

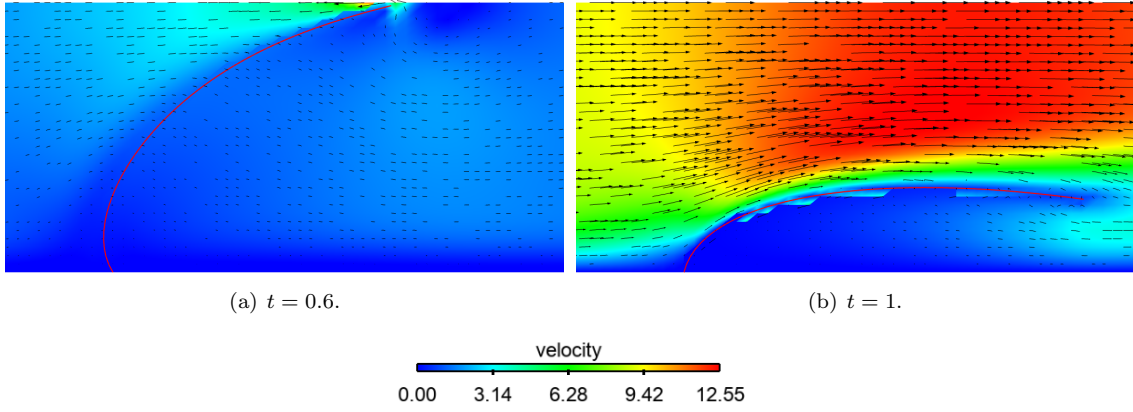


Figure 10: Velocity magnitude snapshots.

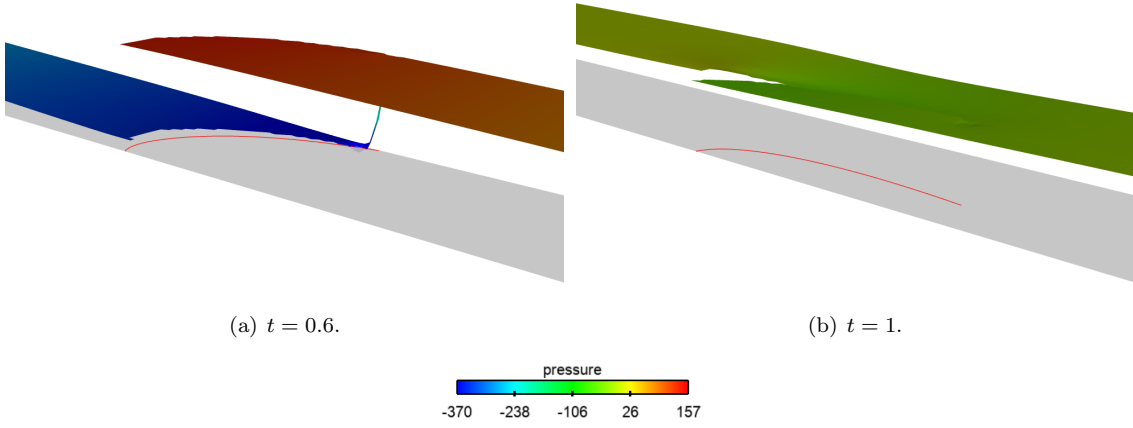


Figure 11: Pressure elevation snapshots.

$t = 0.6$. At this instant, the valve is in contact with the upper wall and the fluid velocity decreases globally as a consequence of the closing. Contrarily to the idealised valve test without porous layer at the top wall, here, we allow the flow to enter the porous interface at contact. The fluid is transported through the porous layer, from the right side of the domain to the left side. At $t = 1$ the valve is open and far from Σ_p , therefore the fluid flow is reestablished and the velocity increases in the channel. The same comparison is performed in Figures 11(a) and (b) for the pressure. We can see the high pressure jump when the valve is in contact with the wall (Figure 11(a)), while at $t = 1$ the discontinuity between the two sides of the interface is weaker (Figure 11(b)).

We now consider the case in which we insert a thin porous layer on the top contact wall and investigate the impact of $K_\tau = K_n$ on the results. Figure 12 presents the time history of the horizontal, Figure 12 (a), and vertical displacement, Figure 12 (b), at the upper solid point B for different levels of conductivity. The non-penetration condition with the wall can be seen in Figure 12(b), whereas Figure 12(a) shows that the structure is sliding over the top wall. The interface is bouncing for all tests except the cases of $K_\tau = K_n = 1$ and 10^{-1} . In such cases, the structure reaches contact and the fluid flows abundantly into the porous layer, which prevents the release of contact. When the inlet pressure increases, the valve opens and the flow is restored. In all the other tests the interface is bouncing, but with a different reaction time, linked to the conductivity value. There is a slight difference in the first release time, but the more visible differences are on the second bounce. Both, the second contact instant and the final release, are considerably sensitive to the changing in $K_\tau = K_n$. Finally, let notice that taking $K_\tau \rightarrow 0$ and $K_n \rightarrow 0$ we converge to the situation of no porous layer on Σ_p , as we can see in Figure 12.

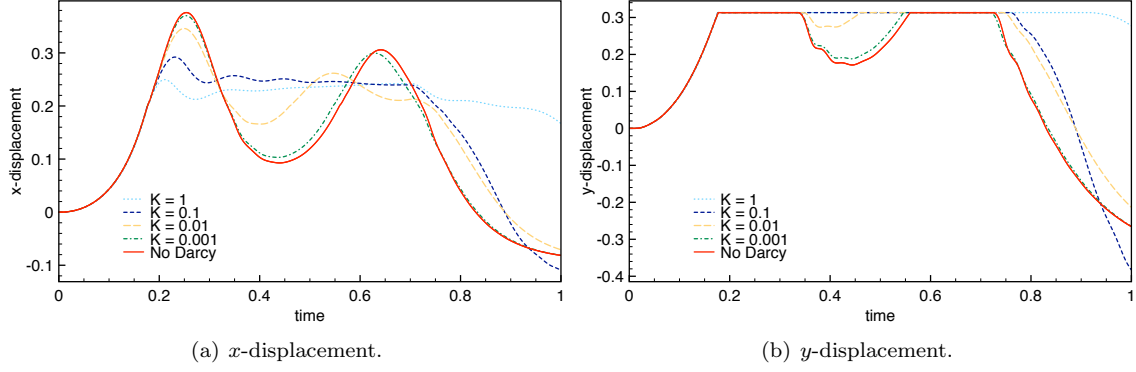


Figure 12: Time evolution of the x and y -displacement for the structure endpoint B .

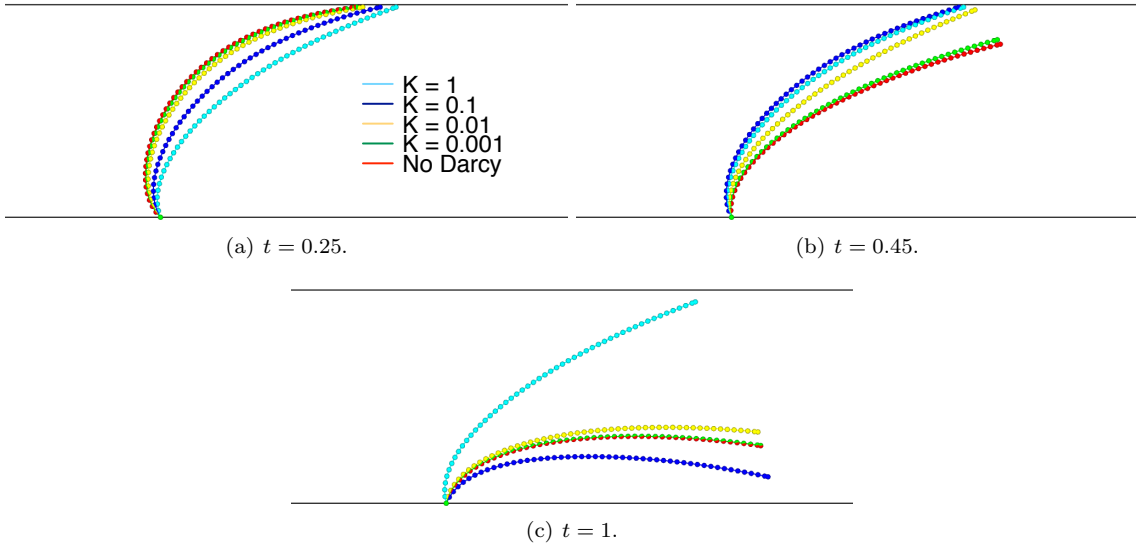


Figure 13: Interfaces location at time $t = 0.25$ (a), $t = 0.45$ (b) and $t = 1$ (c).

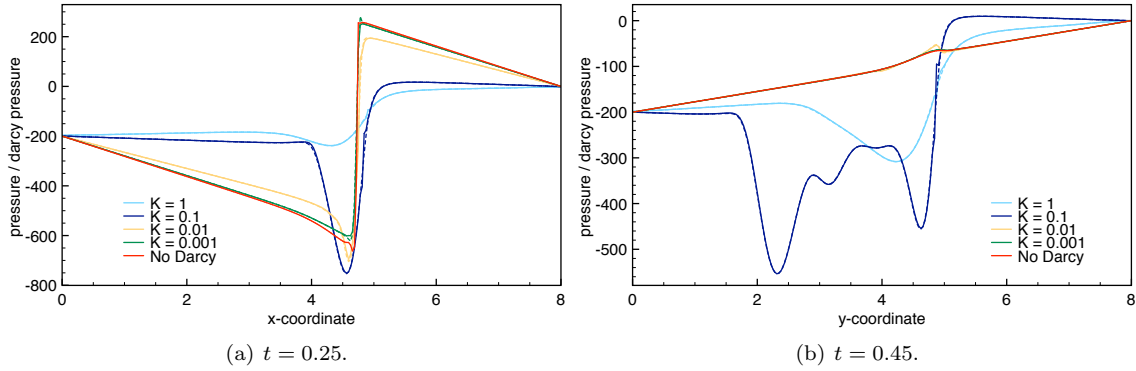


Figure 14: Fluid pressure (continuous line) and porous pressure (dash line) on Σ_p for different value of hydraulic conductivity at time $t = 0.25$ and $t = 0.45$.

Similar observations can be inferred from Figure 13, which shows the interface configuration at time $t = 0.25$ (during contact), $t = 0.45$ (after the first release) and $t = 1$ (when the flow is restored). We

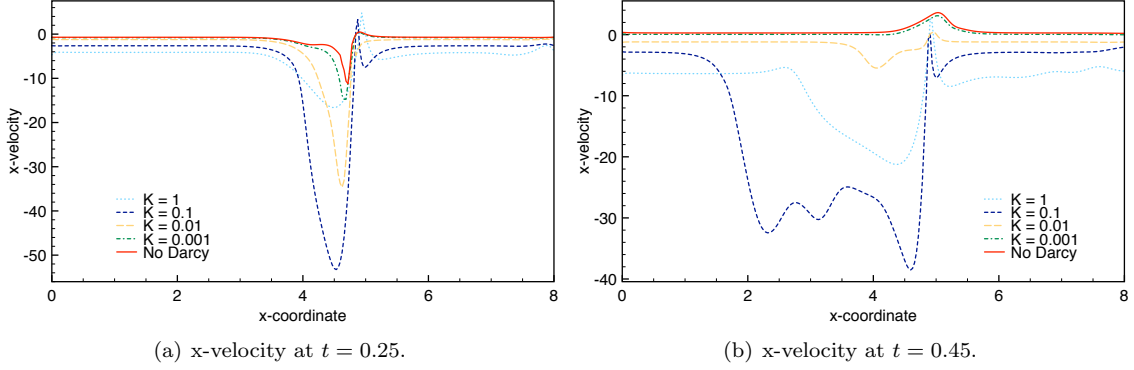


Figure 15: Fluid velocity on Σ_p .

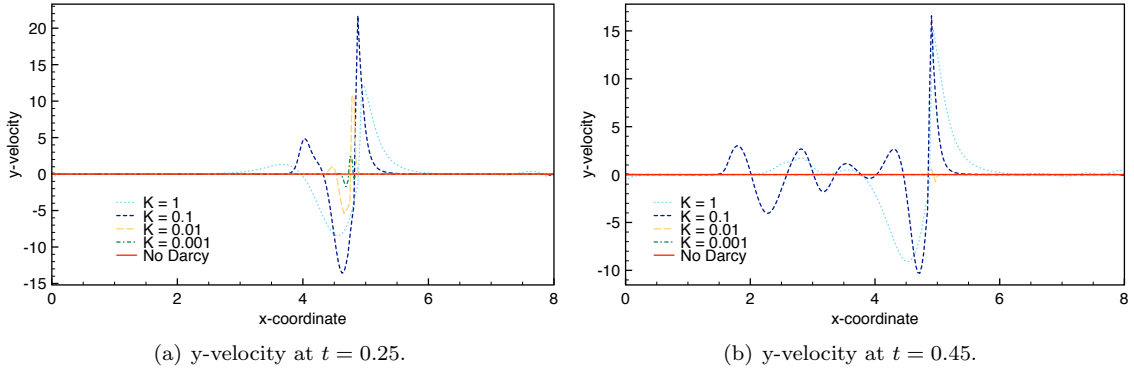


Figure 16: Fluid velocity on Σ_p .

can see that for $K_\tau = K_n = 1$ and 10^{-1} the valve does not bounce, but it only releases once the inlet pressure increases (see Fig. 13(c)). Decreasing the conductivity of the porous medium increases the structure sliding at contact (see Fig. 13(a)) and the bouncing force applied on the structure (see Fig. 13(b)).

Figure 14 displays the fluid pressure (continuous line) and the porous pressures (dashed line) at time $t = 0.25$ and $t = 0.45$. As expected, both pressures remain close. At time $t = 0.25$ the structure is in contact with the upper wall, therefore there is a high pressure gradient that decreases by increasing the conductivity.

Figure 15 shows the fluid x -velocity along the porous layer Σ_p at two different instants. As we can see, the horizontal velocity is not zero also during contact as effect of the porous layer. As expected, the higher the conductivity the greater is the velocity magnitude and a larger area of the porous layer is leaking or pushing fluid inside the domain. In Figure 16 we report the fluid y -velocity on Σ_p . The effect is more localised near the contact area except for cases of $K_\tau = K_n = 1, 0.1$, where the porous layer is still leaking and entering also far from the contact area.

We now explore the results when variations on the porous thickness ε_p are considered. The porous hydraulic conductivity is taken $K_\tau = K_n = 10^{-3}$. We explore results for $\varepsilon_p \in \{10^{-i}\}_{i=1}^4$. The outcome is shown in Figure 17. For $\varepsilon_p \rightarrow 0$ the curves converge towards the results of no porous layer on the top wall.

No particular differences are visible at first contact between the structure and the upper wall. During contact, the horizontal velocity is lower for higher values of ε_p , therefore, the bouncing force is also lower. In addition, the higher is ε_p , the later is the first release, the lower is the rebound force and, consequently, the earlier is the second contact and release. For illustration purposes, we report in Figure 18 a zoom of the y -displacement between the first release and the second contact instants.

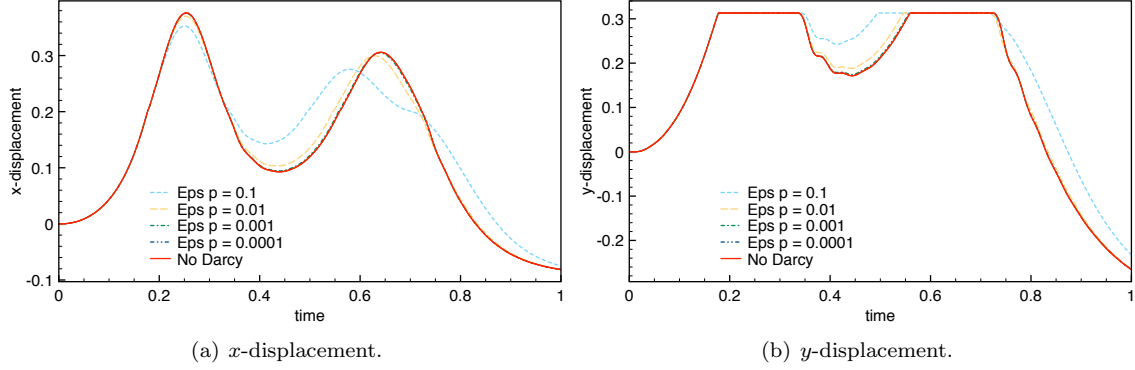


Figure 17: Time evolution of the x -displacement (a) and y -displacement (b) for the structure endpoint B for different values of ε_p

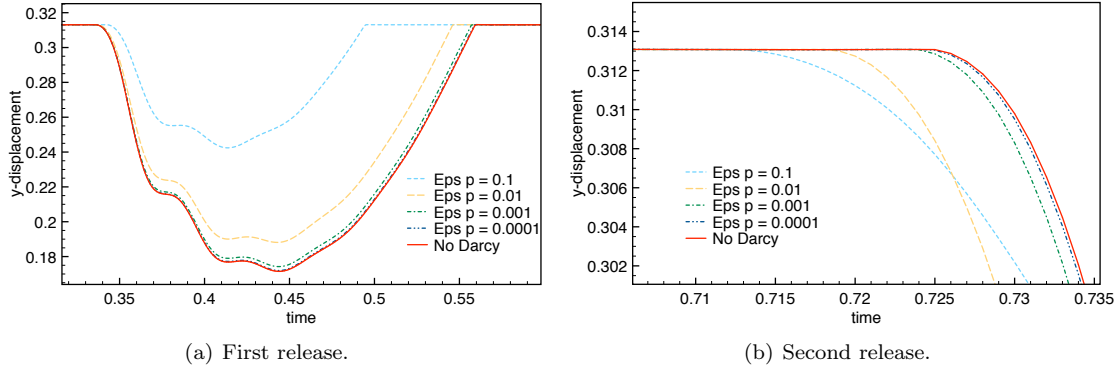


Figure 18: Time evolution of the y -displacement for the structure endpoint B , between first release and second contact (a) and after second release (b).

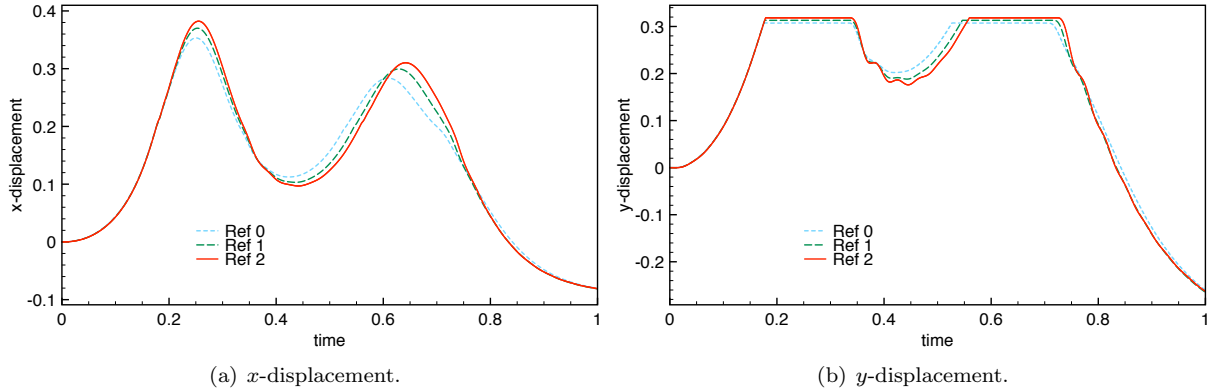


Figure 19: Time evolution of the x -displacement (a) and y -displacement (b) for the structure endpoint B , with different levels of refinement.

Refinement in space and time We explore the convergence behavior taking three levels of space and time refinement, namely $(\delta t, h) \in \{2 \cdot 10^{-3} \cdot 2^{-i}, 0.07 \cdot 2^{-i}\}_{i=0}^2$. The coarser fluid and solid meshes are made of 5 120 triangles and 26 segments, respectively. The second meshes consists of 20 480 triangles and 50 edges, while the finest one has 81 920 triangles and 102 segments. The porous conductivity is chosen $K_\tau = K_n = 10^{-3}$, and the contact relaxation parameter $\varepsilon_h = \varepsilon_h(h)$, chosen $\varepsilon_h \in \{0.02 \cdot 2^{-i}\}_{i=0}^2$.

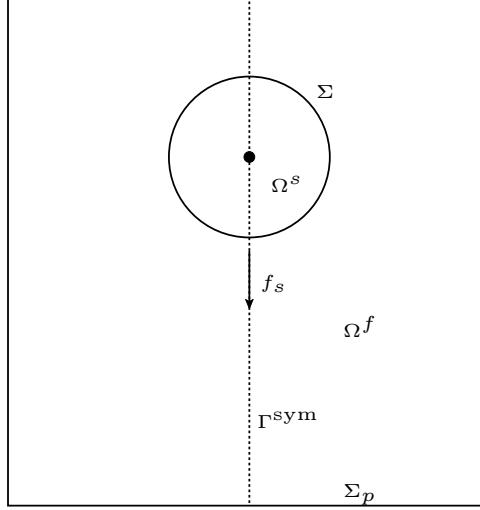


Figure 20: Configuration of the numerical example with the falling ball. The computational domain is reduced to the right half due to symmetry on the axis Γ^{sym} .

We show in Figure 19 the results with these three refinement levels. We observe that the bouncing height is lower for the coarser mesh and that the intermediate level of refinement provides a reasonable approximation. We can also observe that, due to different contact relaxation parameters, contact and release occur at different instants and heights.

4.3 Falling and bouncing elastic ball

In this section, we consider the example of a falling and bouncing elastic ball in a cylinder, which is filled with a water-glycerin mixture. As we are interested in a detailed numerical study, we restrict ourselves to the two-dimensional case here and consider a box of size $6\text{cm} \times 7.5\text{cm}$. The ball has a radius of 1cm and is kept initially at rest at a distance of 4cm from the bottom. The ball falls down due to gravity $f_s = -9.81 \frac{\text{m}}{\text{s}^2}$ and bounces back after the impact. Due to symmetry, we can reduce the computational domain to the right half by imposing symmetry boundary conditions on the midplane Γ^{sym} , see Figure 20.

We use a Fully Eulerian approach to solve the coupled problem, as described in Section 3.2. For simplicity, we consider here a linear elastic material, where the Cauchy stress tensor σ_s is given by

$$\sigma_s(d) = 2\mu_s E(d) + \lambda_s \text{tr}(E(d))I, \quad E(d) = \frac{1}{2} (\nabla d + \nabla d^T),$$

with Lamé parameters $\lambda_s = 7.64 \cdot 10^6 \frac{\text{kg}}{\text{m s}^2}$ and $\nu_s = 1.04 \cdot 10^6 \frac{\text{kg}}{\text{m s}^2}$.

For time discretisation, we use a variant of the backward Euler method, namely a modified dG(0) time-stepping, see [Frei and Richter, 2017b, Frei and Richter, 2017a]. We start with a time-step size of $\delta t = 2 \cdot 10^{-3}\text{s}$, which is reduced in a stepwise procedure up to the impact, where a small time-step size of $\delta t = 1.25 \cdot 10^{-4}\text{s}$ is reached.

The (kinematic) viscosity of the water-glycerol mixture is $\mu_f = 7 \cdot 10^{-6} \frac{\text{m}}{\text{s}^2}$, the density $\rho_f = 1141 \frac{\text{kg}}{\text{m}^3}$ and the solid density $\rho_s = 1351 \frac{\text{kg}}{\text{m}^3}$. Unless stated differently the parameters in the porous medium are chosen as $\epsilon_p = 10^{-4}$ and $K = K_n = K_\tau = 10^{-2}$ and the numerical contact parameters are $\gamma_c = 30\lambda_s$ and $\epsilon_g = \frac{h}{4}$. For the Navier-Stokes-Darcy coupling, we use the Beavers-Joseph-Saffman condition in (9) with $\alpha = 1$. All the results have been obtained with the finite element library Gascoigne3d [Becker et al.,]. We use a structured coarse grid \mathcal{T}_{2h} , which is highly refined close to Σ_p with 3 201 vertices in total (unless specified differently). In Figure 21, we illustrate the vertical velocities u_y and \dot{d}_y of the falling ball at 6 instances of time.

Variation of the conductivity K In Figure 22 we compare the minimum distance to the ground during the fall and before and after the impact for different conductivities K with results obtained without a porous model ("No Darcy"), using either a full slip ($\sigma_{f,\tau} = 0$) or a Navier-slip condition $\sigma_{f,\tau} = \frac{\alpha}{\sqrt{K_\tau \epsilon_p}}$ with $\alpha = 1$ on Σ_p . Note that in the latter case this is exactly the same tangential condition which

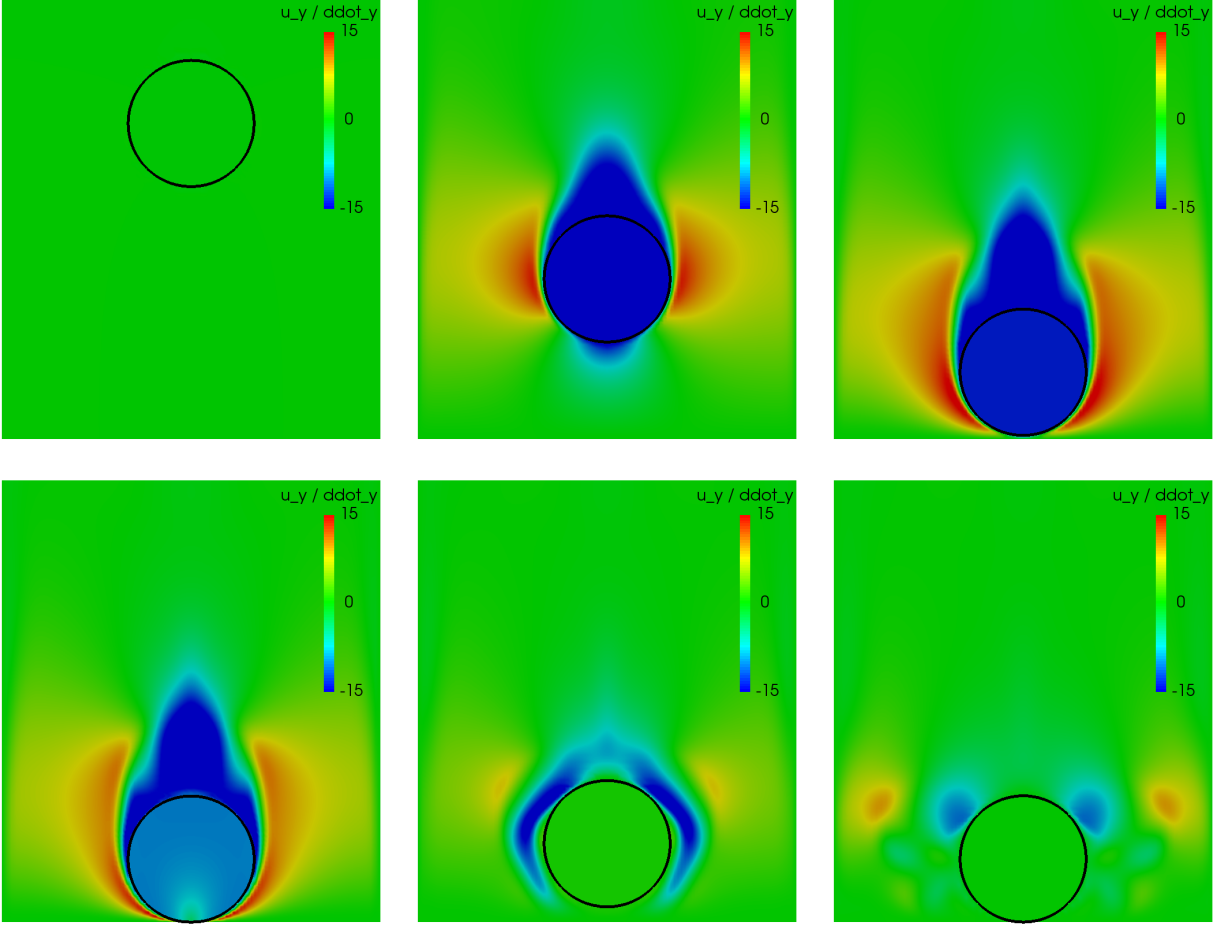


Figure 21: Illustration of the vertical velocities in the falling ball example at $t = 0, 0.28, 0.378$ (top, left to right) and $t = 0.382, 0.47$ and 0.63 (bottom).

is imposed by the Beavers-Joseph-Saffman coupling. There, the normal velocity $\mathbf{u} \cdot \mathbf{n}$ is however not necessarily zero, as the flow can enter into the porous medium.

Depending on K , the ball bounces 4 or 5 times within the time interval $[0, 0.8s]$ with different bouncing heights (top right). The last bounces are barely visible in the graphs shown here due to a very small bouncing height. Moreover, we observe for $K \rightarrow 0$ that the results converge towards the results obtained with a Navier-slip-boundary conditions ("No Darcy"), the curve for $K = 10^{-4}$ showing no visible differences. For larger K the curves get slightly closer towards the results for a pure slip boundary condition.

Concerning the time of impact (bottom left of Fig. 22), we observe that the impact happens slightly later, the smaller the conductivity K . The latest impact is observed for $K = 10^{-4}$ and the pure Navier-slip condition ("No Darcy"). This dependence on K is expected, as the resistive fluid forces that act against the contact are higher for smaller conductivities. The earliest impact is observed for the pure slip condition, followed by $K = 1$. Moreover, we observe that a small distance of about $4.3 \cdot 10^{-5}m$, which lies slightly below the imposed gap distance of $\epsilon_g = 5 \cdot 10^{-5}m$, remains in all cases.

From the upper right picture we can infer the bouncing height depending on K . It holds that the earlier the impact, the higher the impact velocity and hence, we observe a larger bouncing height. Consequently, we observe the largest bounce for pure slip-conditions, followed by $K = 1$, and the smallest one for pure no-slip conditions and $K = 10^{-4}$.

On the bottom right of Figure 22 we show the corresponding vertical velocity \dot{d}_y within the elastic ball, averaged in space. We see that the absolute value of the upwards velocity after the first impact is by more than 30% smaller than the absolute value of the impact velocity in all cases, which shows the

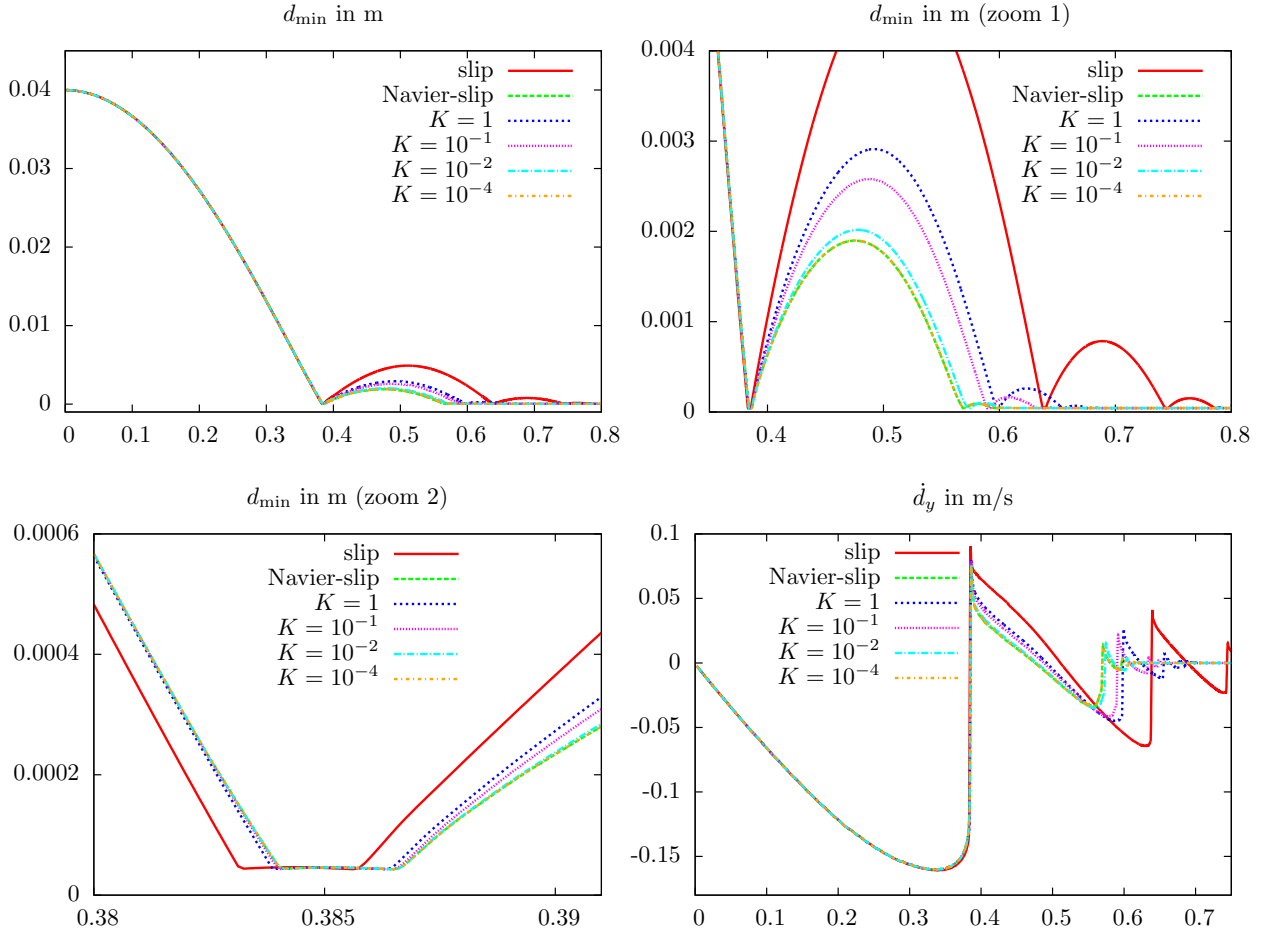


Figure 22: Minimal distance d_{\min} to the ground over time for different conductivities K and compared to pure slip and no-slip conditions on the lower boundary. After the curve over the full time interval $[0, 0.8s]$ on the top left, two different zooms are provided to illustrate the bounces (top right) and the time of impact (bottom left). *Bottom right:* Space-averaged vertical velocity of the elastic ball over time.

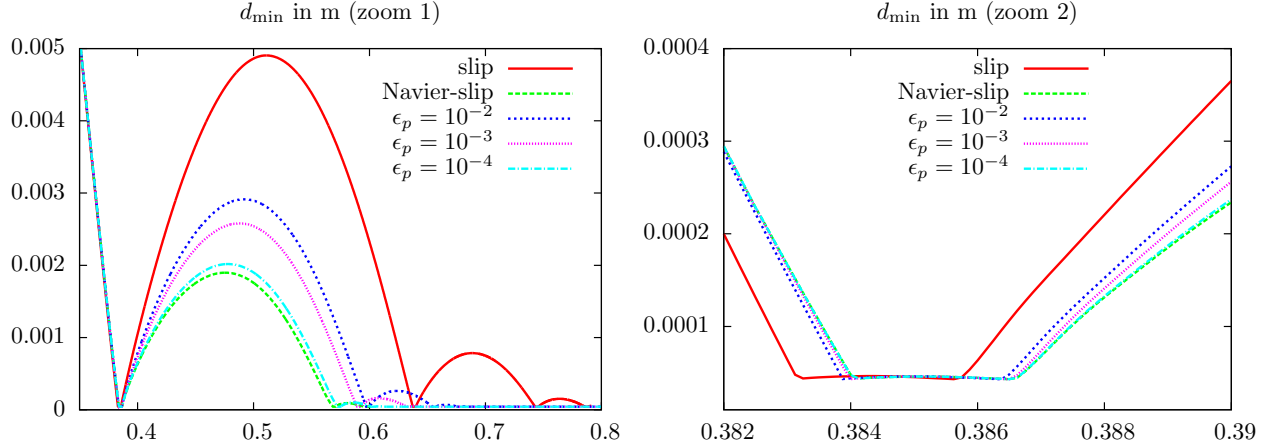


Figure 23: Minimal distance d_{\min} to the ground over time for different thicknesses ϵ_p of the porous layer and compared to pure slip and no-slip conditions on the lower boundary.

dissipative impact of the fluid.

Variation of ϵ_p In Figure 23 we vary the thickness ϵ_p of the porous layer. We obtain 3 to 5 bounces with different heights depending on ϵ_p . For $\epsilon_p \rightarrow 0$, the curves converge towards the results for a pure Navier-slip condition ("No Darcy"), as the first equation in (9) implies $\mathbf{u} \cdot \mathbf{n} \rightarrow 0$. This is also what one expects from the physical model, as a smaller porous layer allows less fluid to diffuse through the layer. In the curve on the right of Figure 23, we see that the contact happens earlier the larger ϵ_p is. This can again be explained by the smaller resistance of the fluid "against" the contact, when this is allowed to escape through the porous layer. The larger impact velocity for larger ϵ_p has again the effect that the bounce is higher for larger ϵ_p .

Variation of the contact parameter γ_c In Figure 24, we illustrate the influence of the contact parameter γ_c . As one would expect the violation of the relaxed contact condition is larger for a smaller γ_c , see the plot on the top right. For $\gamma_c \geq 10\lambda_s$ the curves are almost identical.

On the bottom, we show the contact force $\gamma_c[P_{\gamma_c}]_+$, which appears on the right-hand side of (17), for the first four bounces. We see that the values of the force are almost independent of the chosen contact parameter. While for the smallest contact parameter $\gamma_c = 0.1\lambda_s$ the contact times are slightly altered, there is (almost) no visible difference between the results for $\gamma_c = 10\lambda_s$ and $100\lambda_s$.

Time discretisation In Figure 25, we investigate the influence of the time-step size δt within and around the contact interval. In each simulation we start with a time-step of $\delta t = 2 \cdot 10^{-3}$ at $t = 0$, which is decreased successively by a factor of 2 depending on the distance to the ground. We see that a very small time-step is necessary to capture the contact dynamics. While for the largest time-step $\delta t_{\min} = 1.25 \cdot 10^{-4}$, the bounce is considerably reduced compared to the smaller time-step sizes, the curves seem to converge for $\delta t_{\min} \rightarrow 0$. The reason for the deviation can be deduced from the right plot, which shows that for $\delta t_{\min} = 1.25 \cdot 10^{-4}$ the time of impact and release, where the curve shows a kink (i.e. the solution is non-smooth), is not captured accurately.

Space discretisation In Figure 26 we investigate the convergence behaviour under refinement of the finite element mesh. We fix the minimal time-step to $\delta t_{\min} = 3.125 \cdot 10^{-5}$ and consider a coarse mesh with a maximum cell size of $h \approx 0.175\text{cm}$ and 3 201 vertices and two finer meshes with 12 545 and 49 665 vertices that are constructed from the coarse mesh by global mesh refinement. We observe that the results both concerning minimal distance and vertical velocity are relatively close, even on the coarser mesh level, with an excellent agreement of the results on the finer meshes.

Comparison with a pure no-slip boundary condition In Figure 27, we compare the approach presented in this paper with a simple relaxed contact approach without porous medium ("No Darcy"),

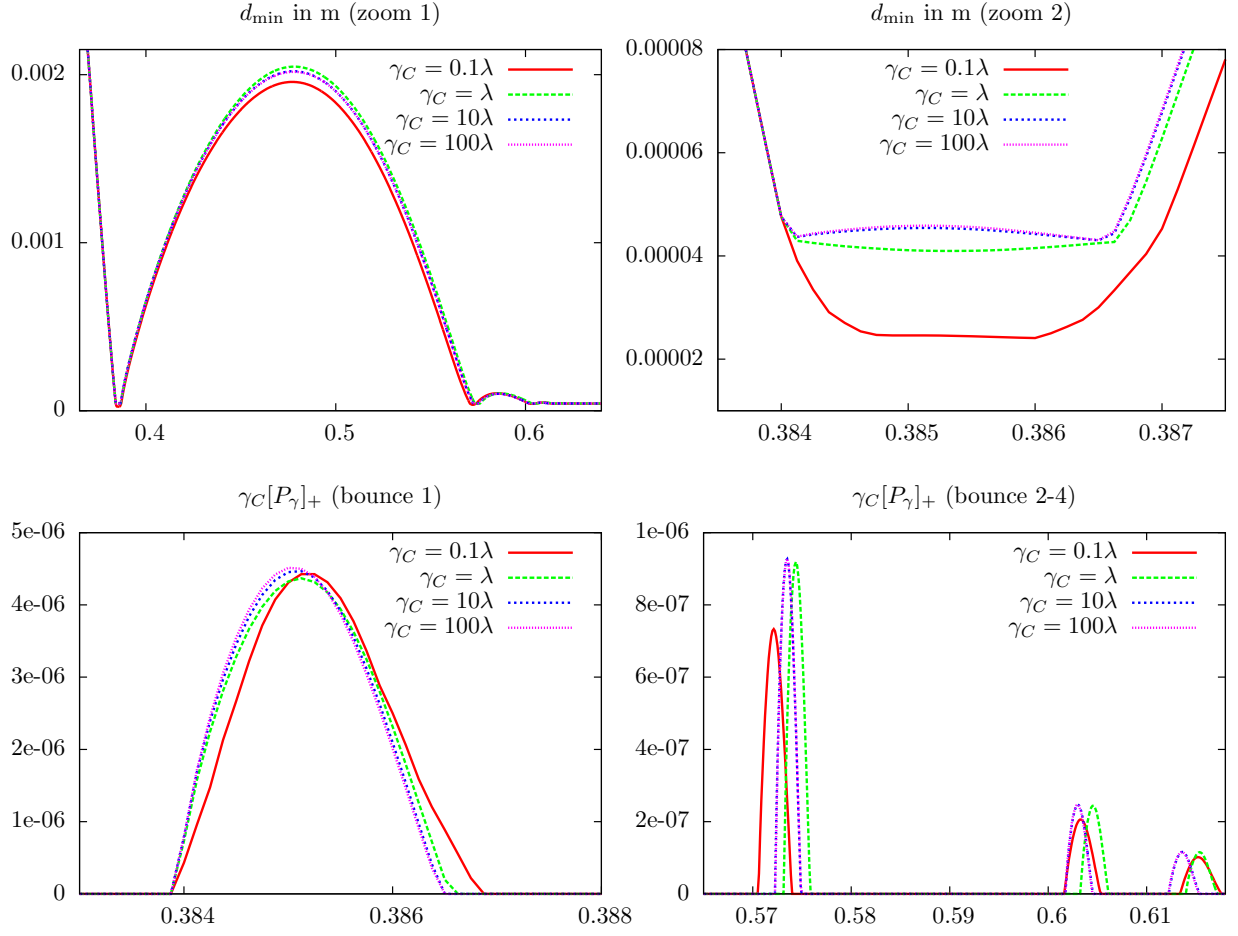


Figure 24: *Top:* Minimal distance d_{\min} to the ground over time for different contact parameters γ_C . *Bottom:* Contact force $\gamma_C[P_\gamma]_+$ over time for the first bounce (*left*) and the second to fourth bounce (*right*).

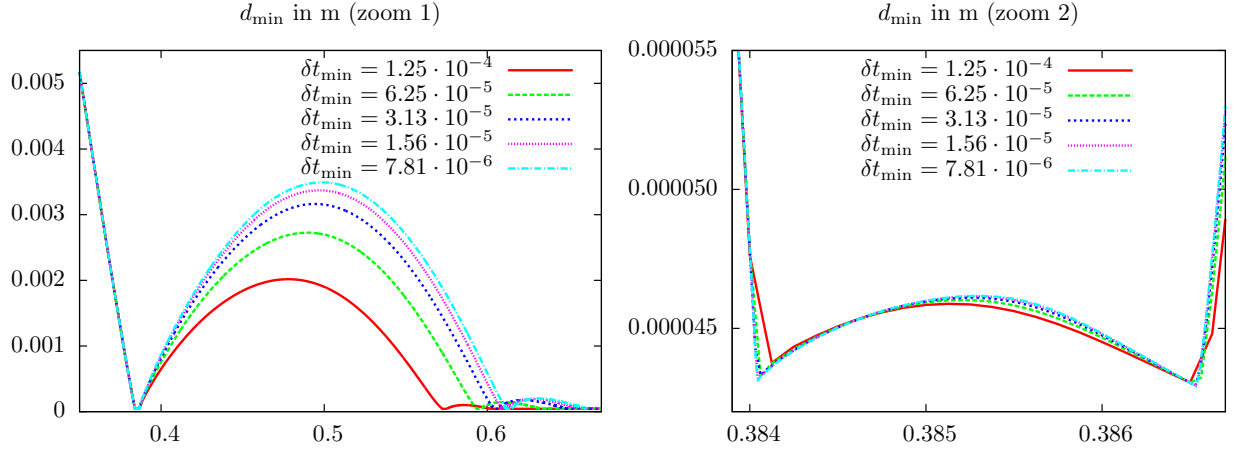


Figure 25: Minimal distance d_{\min} to the ground during the first two bounces (*left*) and at the first impact period (*right*) for different minimal time-step sizes δt_{\min} .

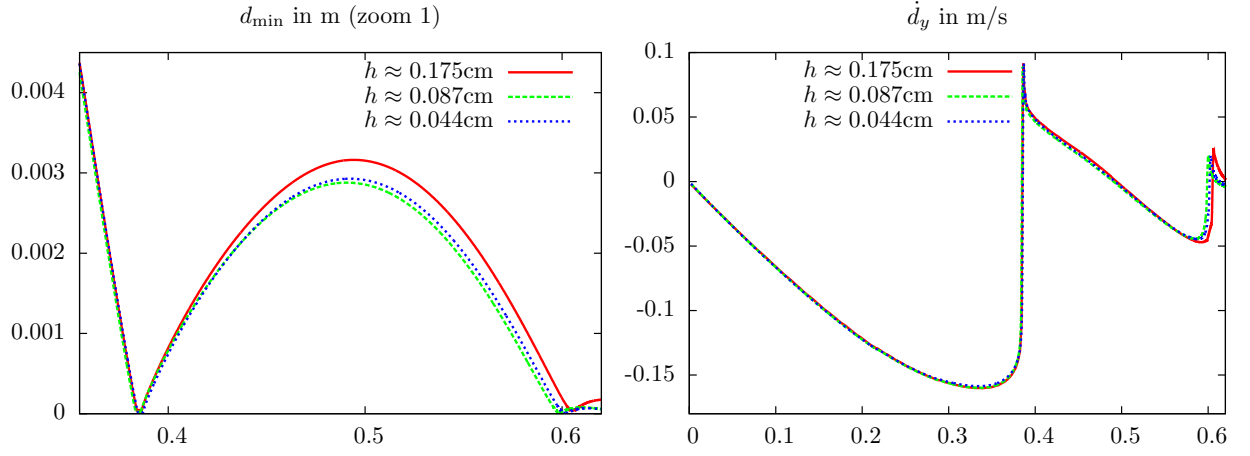


Figure 26: Minimal distance d_{\min} to the ground (left) and space-averaged solid velocity (right) over time on different mesh levels.

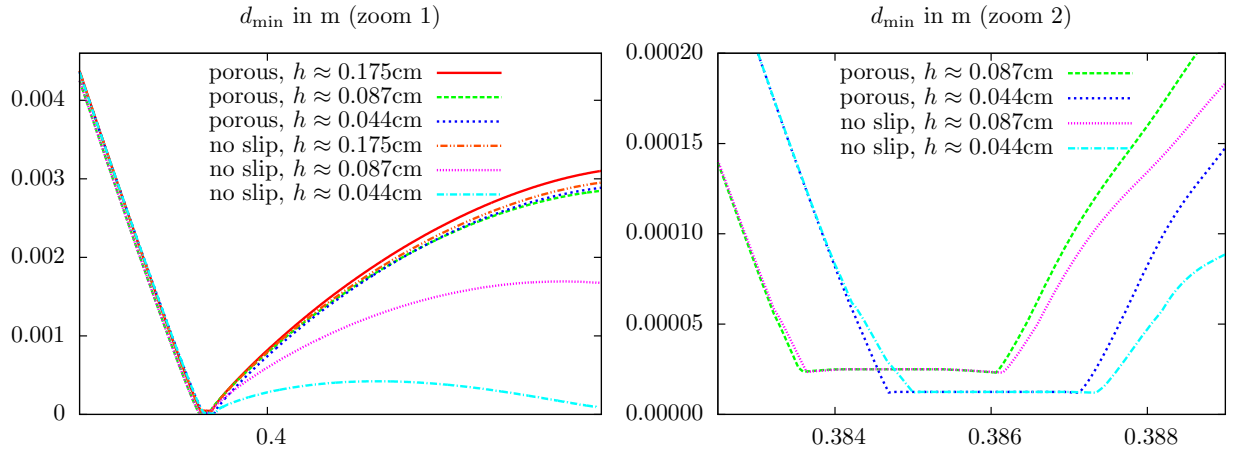


Figure 27: Comparison of the contact approach with a porous layer with pure no-slip ("No Darcy") conditions. Minimal distance d_{\min} to the ground over time on different mesh levels and two different zooms.

h	Porous		no-slip		Navier-slip	
	$-\bar{\dot{d}}_y(t_i)$	$\bar{\dot{d}}_y(t_r)$	$-\bar{\dot{d}}_y(t_i)$	$\bar{\dot{d}}_y(t_r)$	$-\bar{\dot{d}}_y(t_i)$	$\bar{\dot{d}}_y(t_r)$
$1.75 \cdot 10^{-3}$	$1.12 \cdot 10^{-1}$	$8.87 \cdot 10^{-2}$	$1.11 \cdot 10^{-1}$	$8.81 \cdot 10^{-2}$	$1.11 \cdot 10^{-1}$	$8.81 \cdot 10^{-2}$
$8.77 \cdot 10^{-2}$	$1.05 \cdot 10^{-1}$	$8.48 \cdot 10^{-2}$	$9.74 \cdot 10^{-2}$	$7.59 \cdot 10^{-2}$	$9.74 \cdot 10^{-2}$	$7.60 \cdot 10^{-2}$
$4.39 \cdot 10^{-2}$	$1.03 \cdot 10^{-1}$	$8.91 \cdot 10^{-2}$	$7.25 \cdot 10^{-2}$	$5.98 \cdot 10^{-2}$	$7.26 \cdot 10^{-2}$	$5.98 \cdot 10^{-2}$

Table 1: Spatially averaged velocity $\bar{\dot{d}}_y(t) := |\Omega_s(t)|^{-1} \int_{\Omega_s(t)} \dot{d}_y(t) dx$ of the ball at the time of impact $t = t_i$ and at the time of release $t = t_r$ for relaxed contact algorithms with a porous medium model and pure no-slip or Navier-slip conditions on Σ_p on 3 different mesh levels.

where a no-slip condition (resp. a Navier-slip condition) is imposed for the fluid on the bottom wall Σ_p . The no-slip condition is the boundary condition, which is typically used for viscous fluids in absence of contact. First, we note that the curves for the no-slip condition and the Navier-slip condition with (small) slip-length $\left(\frac{\alpha}{\sqrt{K_\tau \epsilon_p}}\right)^{-1}$ are almost identical. For this reason the latter curves are omitted in the following graphs.

As observed before, we see in the left picture that the curves obtained with the porous medium approach converge towards a certain bouncing height for $h \rightarrow 0$. Using a no-slip condition on Σ_p , the bounce get smaller and smaller and it is to be expected that for $h \rightarrow 0$ no bounce takes place at all (which is in agreement with the theoretical works on Navier-Stokes and contact [Hesla, 2004, Hillaire, 2007, Gerard-Varet et al., 2015]). The reason can be inferred from the zoom given on the right of Fig. 27, where we see that the fall is slowed down significantly right before the impact, while the curves for the two variants showed very good agreement until a distance of around 10^{-4} is reached. The reason are the strong fluid forces, in particular the pressure, that act against contact, when a pure no-slip condition is used. The finer the mesh, the better these forces are resolved. Interestingly, the results on the coarsest mesh ($h \approx 0.175$) show still a reasonable agreement, which might indicate that (only) on a very coarse mesh no-slip conditions could still yield physical results within a relaxed contact approach.

Finally, we show in Table 1 the spatially-averaged velocity of the solid at the time of impact t_i and the time of release t_r . Here we see quantitatively that the impact velocity is significantly reduced on the finer mesh levels when using a no-slip condition and thus, a much smaller rebound results.

5 Conclusion

We have introduced a physically consistent model to describe fluid-structure interactions with contact including seepage. For the latter a Darcy model is used on a thin porous layer of infinitesimal thickness. The approach can be used in a variety of different physical and numerical settings, including thick- and thin-walled solids, Eulerian or immersed (mixed-coordinate) descriptions, unfitted or fitted finite element discretisations, etc.

The numerical results show that the approach is numerically stable and (relatively) insensitive to variations of the numerical parameters, such as γ_c . The model parameters ϵ_p and K of the porous layer need to be chosen depending on the application, e.g., the surface properties of the contacting bodies. Moreover, the results indicate convergence in both space and time. The time-step δt_{\min} needs to be chosen very small in and around the contact interval to resolve the contact dynamics accurately.

Due to the relaxation of the contact conditions the approach is relatively easy to implement, in particular in comparison to approaches where a full topology change in the discrete fluid domain takes place and small numerical errors can lead to technical issues like unphysical "islands of fluid" appearing within the contact area, see [Ager et al., 2020].

Future work might focus on the extension to contact between multiple elastic bodies and on further developments within the time discretisation schemes on moving (sub-)domains, including for example adaptive strategies for the time steps δt .

Acknowledgments

EB was partially supported by the EPSRC grants EP/P01576X/1 and EP/T033126/1. The second and fourth authors were partially supported by the French National Research Agency (ANR), through the

References

- [Ager et al., 2019] Ager, C., Schott, B., Vuong, A.-T., Popp, A., and Wall, W. A. (2019). A consistent approach for fluid-structure-contact interaction based on a porous flow model for rough surface contact. *Internat. J. Numer. Methods Engrg.*, 119(13):1345–1378.
- [Ager et al., 2020] Ager, C., Seitz, A., and Wall, W. A. (2020). A consistent and versatile computational approach for general fluid-structure-contact interaction problems. *Int J Numer Methods Eng.* online first: <https://onlinelibrary.wiley.com/doi/abs/10.1002/nme.6556>.
- [Alart and Curnier, 1991] Alart, P. and Curnier, A. (1991). A mixed formulation for frictional contact problems prone to Newton like solution methods. *Comput Methods Appl Mech Eng*, 92(3):353–375.
- [Alauzet et al., 2015] Alauzet, F., Fabrèges, B., Fernández, M., and Landaजूela, M. (2015). Nitsche-xfem for the coupling of an incompressible fluid with immersed thin-walled structures. *Comput Methods Appl Mech Eng*, 301.
- [Alauzet et al., 2016] Alauzet, F., Fabrèges, B., Fernández, M. A., and Landaजूela, M. (2016). Nitsche-XFEM for the coupling of an incompressible fluid with immersed thin-walled structures. *Computer Methods in Applied Mechanics and Engineering*, 301:300–335.
- [Babuška et al., 2004] Babuška, I., Banarjee, U., and Osborn, J. E. (2004). Generalized finite element methods: Main ideas, results, and perspective. *Int J Computat Methods*, 1:67–103.
- [Becker et al.,] Becker, R., Braack, M., Meidner, D., Richter, T., and Vexler, B. The finite element toolkit Gascoigne3d.
- [Boilevin-Kayl et al., 2019] Boilevin-Kayl, L., Fernández, M. A., and Gerbeau, J.-F. (2019). A loosely coupled scheme for fictitious domain approximations of fluid-structure interaction problems with immersed thin-walled structures. *SIAM J. Sci. Comput.*, 41(2):B351–B374.
- [Burman, 2010] Burman, E. (2010). Ghost penalty. *C. R. Math. Acad. Sci. Paris*, 348(21-22):1217–1220.
- [Burman et al., 2015] Burman, E., Claus, S., Hansbo, P., Larson, M. G., and Massing, A. (2015). Cut-FEM: discretizing geometry and partial differential equations. *Internat. J. Numer. Methods Engrg.*, 104(7):472–501.
- [Burman and Fernández, 2014] Burman, E. and Fernández, M. A. (2014). An unfitted Nitsche method for incompressible fluid–structure interaction using overlapping meshes. *Comput Methods Appl Mech Eng*, 279:497–514.
- [Burman et al., 2020a] Burman, E., Fernández, M. A., and Frei, S. (2020a). A Nitsche-based formulation for fluid-structure interactions with contact. *ESAIM: M2AN*, 54(2):531–564.
- [Burman et al., 2021] Burman, E., Fernández, M. A., Frei, S., and Gerosa, F. M. (2021). 3D-2D Stokes-Darcy coupling for the modelling of seepage with an application to fluid-structure interaction with contact. to appear in: Proceedings of Enumath 2019, arXiv e-print: 1912.08503.
- [Burman et al., 2006] Burman, E., Fernández, M. A., and Hansbo, P. (2006). Continuous interior penalty finite element method for Oseen’s equations. *SIAM J. Numer. Anal.*, 44(3):1248–1274.
- [Burman et al., 2020b] Burman, E., Frei, S., and Massing, A. (2020b). Eulerian time-stepping schemes for the non-stationary stokes equations on time-dependent domains.
- [Burman et al., 2017] Burman, E., Hansbo, P., Larson, M. G., and Stenberg, R. (2017). Galerkin least squares finite element method for the obstacle problem. *Computer Methods in Applied Mechanics and Engineering*, 313(Supplement C):362 – 374.
- [Chouly and Hild, 2012] Chouly, F. and Hild, P. (2012). On convergence of the penalty method for unilateral contact problems. *Appl Numer Math*, 65.
- [Chouly and Hild, 2013] Chouly, F. and Hild, P. (2013). A Nitsche-based method for unilateral contact problems: numerical analysis. *SIAM J. Numer. Anal.*, 51(2):1295–1307.
- [Cottet et al., 2008] Cottet, G.-H., Maitre, E., and Milcent, T. (2008). Eulerian formulation and level set models for incompressible fluid-structure interaction. *ESAIM: M2AN*, 42(3):471–492.
- [Di Pietro and Ern, 2012] Di Pietro, D. and Ern, A. (2012). *Mathematical aspects of discontinuous Galerkin methods*, volume 69 of *Mathematics & Applications*. Springer, Heidelberg.

- [Dunne, 2006] Dunne, T. (2006). An Eulerian approach to fluid–structure interaction and goal-oriented mesh adaptation. *Int J Numer Methods Fluids*, 51(9–10):1017–1039.
- [Elliott and Ranner, 2013] Elliott, C. M. and Ranner, T. (2013). Finite element analysis for a coupled bulk-surface partial differential equation. *IMA J. Numer. Anal.*, 33(2):377–402.
- [Frei, 2016] Frei, S. (2016). *Eulerian finite element methods for interface problems and fluid-structure interactions*. PhD thesis, Heidelberg University. <http://www.ub.uni-heidelberg.de/archiv/21590>.
- [Frei, 2019] Frei, S. (2019). An edge-based pressure stabilization technique for finite elements on arbitrarily anisotropic meshes. *Int J Numer Methods Fluids*, 89(10):407–429.
- [Frei et al., 2020] Frei, S., Judakova, G., and Richter, T. (2020). A locally modified second-order finite element method for interface problems. arXiv e-print 2007.13906.
- [Frei and Richter, 2014] Frei, S. and Richter, T. (2014). A locally modified parametric finite element method for interface problems. *SIAM J Numer Anal*, 52(5):2315–2334.
- [Frei and Richter, 2017a] Frei, S. and Richter, T. (2017a). An accurate Eulerian approach for fluid-structure interactions. In Frei, S., Holm, B., Richter, T., Wick, T., and Yang, H., editors, *Fluid-Structure Interaction: Modeling, Adaptive Discretization and Solvers*, Rad Ser Computat Appl Math. Walter de Gruyter, Berlin.
- [Frei and Richter, 2017b] Frei, S. and Richter, T. (2017b). A second order time-stepping scheme for parabolic interface problems with moving interfaces. *ESAIM: M2AN*, 51(4):1539–1560.
- [Gerard-Varet et al., 2015] Gerard-Varet, D., Hillaire, M., and Wang, C. (2015). The influence of boundary conditions on the contact problem in a 3d Navier-Stokes flow. *J Math Pures Appl*, 103:1–38.
- [Gerosa, 2021] Gerosa, F. M. (2021). *Immersed boundary methods for fluid-structure interaction with topological changes*. PhD thesis, Sorbonne Université.
- [Hagemeier et al., 2020] Hagemeier, T., Thévenin, D., and Richter, T. (2020). Settling of spherical, non-wetting particles in a high viscous fluid. arXiv eprint 2009.02250v1.
- [Hansbo et al., 2004] Hansbo, P., Hermansson, J., and Svedberg, T. (2004). Nitsche’s method combined with space-time finite elements for ALE fluid-structure interaction problems. *Comput. Methods Appl. Mech. Engrg.*, 193(39–41):4195–4206.
- [Hesla, 2004] Hesla, T. I. (2004). *Collisions of smooth bodies in viscous fluids: A mathematical investigation*. PhD thesis, University of Minnesota.
- [Hillairet, 2007] Hillairet, M. (2007). Lack of collision between solid bodies in a 2d incompressible viscous flow. *Commun Part Diff Eq*, 32(9):1345–1371.
- [Lehrenfeld and Olshanskii, 2019] Lehrenfeld, C. and Olshanskii, M. (2019). An Eulerian finite element method for pdes in time-dependent domains. *ESAIM: M2AN*, 53(2):585–614.
- [Martin et al., 2005] Martin, V., Jaffré, J., and Roberts, J. (2005). Modeling fractures and barriers as interfaces for flow in porous media. *SIAM J. Sci. Comput.*, 26(5):1667–1691.
- [Massing et al., 2013] Massing, A., Larson, M. G., and Logg, A. (2013). Efficient implementation of finite element methods on nonmatching and overlapping meshes in three dimensions. *SIAM J. Sci. Comput.*, 35(1):C23–C47.
- [Mikelic and Jäger, 2000] Mikelic, A. and Jäger, W. (2000). On the interface boundary condition of Beavers, Joseph, and Saffman. *SIAM J Appl Math*, 60(4):1111–1127.
- [Moës et al., 1999] Moës, N., Dolbow, J., and Belytschko, T. (1999). A finite element method for crack growth without remeshing. *Int J Numer Methods Eng*, 46:131–150.
- [Nield et al., 2006] Nield, D., Bejan, A., et al. (2006). *Convection in porous media*, volume 3. Springer.
- [Peskin, 1972] Peskin, C. S. (1972). Flow patterns around heart valves: a numerical method. *J Comput Phys*, 10(2):252–271.
- [Richter, 2013] Richter, T. (2013). A fully Eulerian formulation for fluid-structure interactions. *J Computat Phys*, 233:227–240.
- [Rockafellar, 1973] Rockafellar, R. T. (1973). A dual approach to solving nonlinear programming problems by unconstrained optimization. *Math. Programming*, 5:354–373.
- [Saffman, 1971] Saffman, P. G. (1971). On the boundary condition at the surface of a porous medium. *Studies Appl Math*, 50(2):93–101.

- [Scholz, 1984] Scholz, R. (1984). Numerical solution of the obstacle problem by the penalty method. *Computing*, 32:297–306.
- [von Wahl et al., 2020] von Wahl, H., Richter, T., Frei, S., and Hagemeier, T. (2020). Falling balls in a viscous fluid with contact: Comparing numerical simulations with experimental data. *arXiv e-prints*, pages arXiv:2011.08691, accepted for publication at Phys Fluids.
- [Zonca et al., 2020] Zonca, S., Antonietti, P. F., and Vergara, C. (2020). A polygonal discontinuous Galerkin formulation for contact mechanics in fluid-structure interaction problems. MOX-Report No. 26/2020, <https://www.mate.polimi.it/biblioteca/add/qmox/26-2020.pdf>.
- [Zonca et al., 2018] Zonca, S., Vergara, C., and Formaggia, L. (2018). An unfitted formulation for the interaction of an incompressible fluid with a thick structure via an XFEM/DG approach. *SIAM J. Sci. Comput.*, 40(1):B59–B84.